References

1 Garrett DM, Conrad GW. Fibroblast-like cells from embryonic chick cornea, heart, and skin are antigenically distinct. Dev Biol 1979;70:50–70.

2 Schor SL, Schor AM. Clonal heterogeneity in fibroblast phenotype: implications for the control of epithelial-mesenchymal interactions. Bioessays 1987;7:200–204.

3 Ronnov-Jessen L, Petersen OW, Koteliansky VE et al. The origin of the myofibroblasts in breast cancer: recapitulation of tumor environment in culture unravels diversity and implicates converted fibroblasts and recruited smooth muscle cells. J Clin Invest 1995;95:859–873.

4 Dugina V, Alexandrova A, Chaponnier C et al. Rat fibroblasts cultured from various organs exhibit differences in alpha-smooth muscle actin expression, cytoskeletal pattern, and adhesive structure organization. Exp Cell Res 1998;238:481–490.

5 Jelaska A, Strehlow D, Korn JH. Fibroblast heterogeneity in physiological conditions and fibrotic disease. Springer Semin Immunopathol 1999;21:385–395.

6 Chang HY, Chi JT, Dudoit S et al. Diversity, topographic differentiation, and positional memory in human fibroblasts. Proc Natl Acad Sci U S A 2002;99:12877–12882.

7 Ferrari G, Cusella-De Angelis G, Coletta M et al. Muscle regeneration by bone marrow-derived myogenic progenitors. Science 1998;279:1528–1530.

8 Shimizu K, Sugiyama S, Aikawa M et al. Host bone-marrow cells are a source of donor intimal smooth- muscle-like cells in murine aortic transplant arteriopathy. Nat Med 2001;7:738–741.

9 Kuznetsov SA, Mankani MH, Gronthos S et al. Circulating skeletal stem cells. J Cell Biol 2001;153:1133–1140.

10 LaBarge MA, Blau HM. Biological progression from adult bone marrow to mononucleate muscle stem cell to multinucleate muscle fiber in response to injury. Cell 2002;111:589–601.

11 Corbel SY, Lee A, Yi L et al. Contribution of hematopoietic stem cells to skeletal muscle. Nat Med 2003;9:1528–1532.

12 Makino S, Fukuda K, Miyoshi S et al. Cardiomyocytes can be generated from marrow stromal cells in vitro. J Clin Invest 1999;103:697–705.

13 Jackson KA, Majka SM, Wang H et al. Regeneration of ischemic cardiac muscle and vascular endothelium by adult stem cells. J Clin Invest 2001;107:1395–1402.

14 Orlic D, Kajstura J, Chimenti S et al. Bone marrow cells regenerate infarcted myocardium. Nature 2001;410:701–705.

15 Petersen BE, Bowen WC, Patrene KD et al. Bone marrow as a potential source of hepatic oval cells. Science 1999;284:1168–1170.

16 Theise ND, Badve S, Saxena R et al. Derivation of hepatocytes from bone marrow cells in mice after radiation-induced myeloablation. Hepatology 2000;31:235–240.

17 Alison MR, Poulsom R, Jeffery R et al. Hepatocytes from non-hepatic adult stem cells. Nature 2000;406:257.

18 Lagasse E, Connors H, Al-Dhalimy M et al. Purified hematopoietic stem cells can differentiate into hepatocytes in vivo. Nat Med 2000;6:1229–1234.

19 Gao Z, McAlister VC, Williams GM. Repopulation of liver endothelium by bone-marrow-derived cells. Lancet 2001;357:932–933.

20 Asahara T, Masuda H, Takahashi T et al. Bone marrow origin of endothelial progenitor cells responsible for postnatal vasculogenesis in physiological and pathological neovascularization. Circ Res 1999;85:221–228.

21 Sata M, Saiura A, Kunisato A et al. Hematopoietic stem cells differentiate into vascular cells that participate in the pathogenesis of atherosclerosis. Nat Med 2002;8:403–409.

22 Prockop DJ. Marrow stromal cells as stem cells for nonhematopoietic tissues. Science 1997;276:71–74.

23 Pittenger MF, Mackay AM, Beck SC et al. Multilineage potential of adult human mesenchymal stem cells. Science 1999;284:143–147.

24 Jiang Y, Jahagirdar BN, Reinhardt RL et al. Pluripotency of mesenchymal stem cells derived from adult marrow. Nature 2002;418:41–49.

25 Iwano M, Plieth D, Danoff TM et al. Evidence that fibroblasts derive from epithelium during tissue fibrosis. J Clin Invest 2002;110:341–350.

26 Ishii G, Sangai T, Oda T et al. Bone-marrow-derived myofibroblasts contribute to the cancer-induced stromal reaction. Biochem Biophys Res Commun 2003;309:232–240.

27 Brittan M, Hunt T, Jeffery R et al. Bone marrow derivation of pericryptal myofibroblasts in the mouse and human small intestine and colon. Gut 2002;50:752–757.

28 Direkze NC, Forbes SJ, Brittan M et al. Multiple organ engraftment by bone-marrow-derived myofibroblasts and fibroblasts in bone-marrow-transplanted mice. STEM CELLS 2003;21:514–520.

29 Hashimoto N, Jin H, Liu T et al. Bone marrow-derived progenitor cells in pulmonary fibrosis. J Clin Invest 2004;113:243–252.

30 Mombaerts P, Iacomini J, Johnson RS et al. RAG-1-deficient mice have no mature B and T lymphocytes. Cell 1992;68:869–877.

31 Sasaki T, Sasaki-Irie J, Penninger JM. New insights into the transmembrane protein tyrosine phosphatase CD45. Int J Biochem Cell Biol 2001;33:1041–1046.

32 Penninger JM, Irie-Sasaki J, Sasaki T et al. CD45: new jobs for an old acquaintance. Nat Immunol 2001;2:389–396.

33 Deschaseaux F, Gindraux F, Saadi R et al. Direct selection of human bone marrow mesenchymal stem cells using an anti-CD49a antibody reveals their $CD45^{med,low}$ phenotype. Br J Haematol 2003;122:506–517.

34 Singer JW, Charbord P, Keating A et al. Simian virus 40-transformed adherent cells from human long-term marrow cultures: cloned cell lines produce cells with stromal and hematopoietic characteristics. Blood 1987;70:464–474.

35 Koumas L, King AE, Critchley HO et al. Fibroblast heterogeneity: existence of functionally distinct Thy 1^+ and Thy 1^- human female reproductive tract fibroblasts. Am J Pathol 2001;159:925–935.

36 Koumas L, Phipps RP. Differential COX localization and PG release in Thy-1^+ and Thy-1^- human female reproductive tract fibroblasts. Am J Physiol Cell Physiol 2002;283:C599–608.

37 Koumas L, Smith TJ, Feldon S et al. Thy-1 expression in human fibroblast subsets defines myofibroblastic or lipofibroblastic phenotypes. Am J Pathol 2003;163:1291–1300.

38 Bucala R, Spiegel LA, Chesney J et al. Circulating fibrocytes define a new leukocyte subpopulation that mediates tissue repair. Mol Med 1994;1:71–81.

39 Abe R, Donnelly SC, Peng T et al. Peripheral blood fibrocytes: differentiation pathway and migration to wound sites. J Immunol 2001;166:7556–7562.

Int. J. Cancer: **117,** 212–220 (2005)

In vivo and *in vitro* characterization of human fibroblasts recruited selectively into human cancer stroma

Genichiro Ishii[1], Takafumi Sangai[1], Takashi Ito[1,2], Takahiro Hasebe[1], Yasushi Endoh[1], Hiroki Sasaki[3], Kenichi Harigaya[4] and Atsushi Ochiai[1,2]*

[1]*Pathology Division, National Cancer Center Research Institute East, Kashiwa, Chiba, Japan*
[2]*Laboratory of Cancer Biology, Department of Integrated Biosciences, Graduate School of Frontier Sciences, University of Tokyo, Kashiwa, Chiba, Japan*
[3]*Genetics Division, National Cancer Center Research Institute, Tokyo, Japan*
[4]*Molecular and Tumor Pathology, Graduate School of Medicine, Chiba University, Chiba, Japan*

Fibroblasts, which are a major component of cancer-induced stroma, can have a significant impact on the progression of adjacent malignant epithelia. To characterize fibroblasts recruited into cancer-induced stroma, we examined the recruitment efficiency of 9 human fibroblast cell lines into experimental tumors generated in immunodeficient mice. Green fluorescence protein (GFP)–labeled fibroblast cell lines and human pancreatic cancer cell line Capan-1 were injected i.p. at different sites; the GFP-labeled cells within xenografts were then analyzed. KM104^{GFP} (bone marrow) and VA-13^{GFP} (lung) were selectively recruited into cancer stroma more efficiently than the other cell lines. KM104^{GFP} cells did not affect tumor volume; however, VA-13^{GFP} cells increased tumor volume by about 2-fold. After 5 cyclic *in vivo* passages of KM104^{GFP} in Capan-1, we selected a subpopulation with an 8.4-fold higher recruitment efficiency (KM104^{GFP}-5G) compared to parental KM104^{GFP}. KM104^{GFP}-5G also exhibited higher chemotaxis and chemoinvasion activity compared to KM104^{GFP} in response to cancer-released chemoattractant(s). Oligonucleotide microarray analysis identified 8 genes with >3-fold upregulation and 6 genes with >3-fold downregulation in KM104^{GFP}-5G. Immunohistochemistry confirmed that fibroblasts recruited into pancreatic cancer stroma strongly expressed carbonic anhydrase IX and keratin-8, whose transcripts were upregulated in KM104^{GFP}-5G by oligonucleotide microarray analysis, whereas their expression in fibroblasts within noncancerous pancreatic stroma were under the detection level. Our results indicate that fibroblast recruitment is not selective with respect to organ origin and that particular fibroblast subpopulations with specific phenotypic characteristics could be recruited efficiently into cancer-induced stroma.

Key words: fibroblast; cancer stroma; recruitment; green fluorescent protein

The invasion process of cancer cells is associated with the generation of specific stroma, called "cancer-induced stroma". The main constituents of cancer-induced stroma are inflammatory cells, including lymphocytes, granulocytes, macrophages, the endothelial cells of blood and lymph vessels, pericytes and fibroblasts. Inflammatory cells and endothelial cells are recruited into cancer stroma and involved in tumor immunity[1–4] and neoangiogenesis,[5,6] respectively. Fibroblasts, which are the major component of stroma, are also recruited and can convert into smooth muscle actin-positive fibroblasts, *i.e.,* myofibroblasts or activated fibroblasts, and produce collagens and extracellular matrix proteins in response to several extracellular stimuli. The paracrine signaling interactions between cancer cells and associated fibroblasts play important roles in tumor formation and progression.[7–9] Experimental evidence of fibroblast recruitment into cancer stroma comes from the demonstration that the tumor microenvironment preferentially promotes engraftment of i.v.-injected bone marrow–derived mesenchymal stem cells.[10] In addition, when β-galactosidase-transduced human fibroblasts were injected i.p. into SCID mice with an ovarian cancer cell line, they preferentially localized within the cancer stroma but not within the normal tissue stroma.[11] Bone marrow–derived fibroblasts contribute to the tumor stromal reaction. We have reported that stroma generated by invasive cancer cells consist of both bone marrow–derived and non-bone marrow–derived activated fibroblasts and that the bone marrow–derived activated fibroblasts were recruited into cancer-induced stroma at a later stage.[12] Furthermore, Direkze *et al.*[13] also described the bone marrow contribution to tumor-associated myofibroblasts and fibroblasts. However, the functional implications of bone marrow–derived fibroblasts for cancer growth remain unclear.

Stromal fibroblasts create a context that promotes tumor progression.[14,15] Furthermore, investigators have found evidence that the proliferative activity of stromal fibroblasts in cancer-induced stroma is closely linked to lymph node and distant organ metastasis[16,17] and that soluble factor secretion by stromal fibroblasts influences tumor progression.[18,19] Elucidation of the mechanism by which fibroblasts are recruited into cancer stroma could lead to new insights into not only the mechanisms of cancer progression but also strategies for cancer treatment.

In the present study, we addressed the efficiency and selectivity of fibroblast recruitment into experimental tumors. First, we analyzed whether fibroblast cell lines derived from different or the same organs could be equally recruited into cancer-induced stroma. We found that recruitment of fibroblasts into cancer stroma is not selective with respect to organ origin. Furthermore, we developed a novel method to obtain a fibroblast cell line with higher recruitment efficiency by repeated *in vivo* passages within cancer stroma. We also found that the biologic phenotype of recruited fibroblasts is distinct from that of nonrecruited fibroblasts.

Material and methods

Animals

Six-week-old female SCID mice (C.B-17 background) were purchased from Clea (Tokyo, Japan) and maintained at the National Cancer Center Research Institute East. All animals were maintained under specific pathogen-free, temperature-controlled environmental conditions throughout the study, in accordance with institutional guidelines. Written approval for all animal experiments (K03-011) was obtained from the local Animal Experiments Committee of the National Cancer Center Research Institute.

Abbreviations: CA IX, carbonic anhydrase IX; GFP, green fluorescent protein; hFB, human fibroblast; HRP, horseradish peroxidase; MFI, mean fluorescence intensity; MMP, matrix metalloproteinase; RT, reverse transcriptase; SCID, severe combined immunodeficiency.

***Correspondence to:** Pathology Division, National Cancer Center Research Institute East, 6-5-1 Kashiwanoha, Kashiwa-City, Chiba 277-8577, Japan. Fax: +81-4-7134-6865. E-mail: aochiai@east.ncc.go.jp

Received 29 July 2004; Accepted after revision 11 March 2005
DOI 10.1002/ijc.21199
Published online 17 May 2005 in Wiley InterScience (www.interscience.wiley.com).

Cell lines and cell cultures

SV-40 transformed human fibroblast cell lines from bone marrow (KM101, 102, 103, 104 and 105) were originally established from an identical male patient, as previously described.[20] These cell lines were cultured in RPMI-1640 medium with 10% heat-inactivated FBS and antibiotics (penicillin and streptomycin). SV-40 transformed fibroblast cell lines from lung (VA-13, IMR-90-SV and MRC-5 SV1 TG1) and skin (W-V) were purchased from Riken (Tsukuba, Japan). These cell lines were cultured in DMEM with 10% heat-inactivated FBS and antibiotics. The human pancreatic cancer cell line Capan-1 was purchased from the ATCC (Rockville, MD). Capan-1 was maintained in RPMI-1640 medium with 20% heat-inactivated FBS and antibiotics. All cells were maintained in a 5% CO_2 incubator at 37°C.

Retroviral transfer of GFP and cell sorting

Recombinant retroviruses were produced by cotransfecting the pMX-GFP vector[21] (kindly provided by Dr. T. Kitamura, University of Tokyo, Tokyo, Japan) and amphotropic helper virus DNA into 293T cells. Human fibroblast cell lines were infected with recombinant retroviruses by culturing in conditioned medium in the presence of polybrene. GFP-positive fibroblast cell lines were further sorted using a FACScaliber sorting system (Becton Dickinson, San Jose, CA).

Xenotransplantation of GFP-labeled human fibroblast cell lines and Capan-1

Capan-1 cells (5×10^6/animal) were injected into the peritoneal cavities of SCID mice. One hour later, 5×10^6 cells of a GFP-labeled fibroblast cell line were injected into each peritoneal cavity at a different injection site. As we did not know when the cellular interactions between human fibroblasts and Capan-1 cells, which are responsible for efficient recruitment into the cancer stroma, occur, we reinjected GFP-labeled fibroblasts on day 14, a week before tumor removal. Animals were killed on day 21 and the tumor masses and other tissues removed. Control mice received only a Capan-1 injection. Another experiment was performed as follows. Capan-1 cells (5×10^6/animal) were injected into the peritoneal cavities of SCID mice on day 0. Next, 5×10^6 cells of GFP-labeled KM104 cells were injected i.p. on day 0, 7 or 14 after the Capan-1 transplantation; animals were killed on day 21. Tumor volume was calculated by the formula volume = (width^2 × length)/2. We measured both tumor volume and tumor wet weight in each sample and confirmed that tumor wet weight was proportional to tumor volume (1.6 ± 0.2 mg/mm^3).

Immunohistochemical and immunofluorescence analysis

Xenografted cancer tissues were fixed in 10% formaldehyde for 1 day. Double immunolabeling was performed on sections using an indirect immunoperoxidase technique followed by an indirect alkaline phosphatase technique. Primary antibodies were a rabbit polyclonal anti-topoisomerase IIα (Novocastra, New Castle-upon-Tyne, UK) at 1:100 dilution and a rabbit polyclonal anti-GFP (Molecular Probes, Eugene, OR) at a 1:1,000 dilution. Tissue sections (5 μm) were treated using a microwave-based antigen retrieval technique with 10 mmol/l citrate buffer (pH 6.0) for 20 min at 90°C. Endogenous peroxidases were inactivated with 3% H_2O_2 in methanol. Sections were incubated for 1 hr with anti-topoisomerase IIα antibody, then with EnVisionTM+System-HRP (Dako, Glostrup, Denmark). Reacted products were stained with diaminobenzidine. Sections were incubated with anti-GFP antibody for 1 hr and then with EnVisionTM+System-AP (Dako). After washing in PBS, the product of the alkaline phosphatase reaction was revealed using 0.5% fuchsin solution.

Double immunofluorescence analysis was performed by sectioning specimens into 3-μm-thick sections and incubating them with the primary antibodies, including rabbit polyclonal anti-GFP-Alexa Fluor 488 (Molecular Probes) at a 1:500 dilution and a mouse monoclonal antihuman cytokeratin (AE1/3, Dako) at a 1:50 dilution. Alexa Fluor 546 antimouse IgG (Molecular Probes) was used as the secondary antibody. Sections were examined using an inverted microscope with an excitation wavelength of 488 nm for Alexa Fluor 488 and 568 nm for Alexa Fluor 546. After mounting, sections were examined using an LSM5 PASCAL confocal imaging system (Carl Zeiss, Oberkochen, Germany). Confocal images were stored as digital files and viewed using Photoshop (Adobe, Mountain View, CA). Surgically resected pancreatic cancer tissues were snap-frozen in liquid nitrogen and stored at −80°C until used. Tissue sections (5 μm) were fixed in 10% formaldehyde for 5 min, and endogenous peroxidases were inactivated with 3% H_2O_2 in methanol. Primary antibodies included a goat polyclonal anti-CA IX (Santa Cruz Biotechnology, Santa Cruz, CA) at a 1:100 dilution and a mouse monoclonal anti-cytokeratin 8 (Dako, Denmark) at a 1:50 dilution. Sections were incubated for 1 hr, followed by the standard ABC technique (Vector, Burlingame, CA).

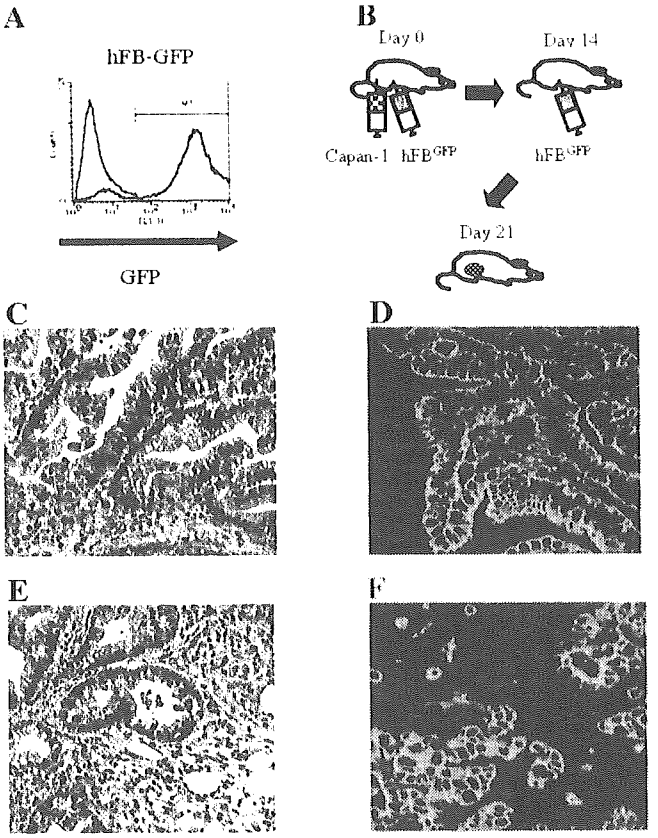

FIGURE 1 – Recruitment of GFP-labeled human fibroblast cell lines into cancer stroma. (*a*) Flow-cytometric analysis of GFP expression in genetically engineered human transformed fibroblast cell lines (hFB^{GFP}). Thin line, KM104 before *in vitro* transduction; thick line, KM104 after GFP transduction. (*b*) Capan-1 (5×10^6/animal) cells were injected into the peritoneal cavities of SCID mice. One hour later, 5×10^6 cells of a GFP-labeled fibroblast cell line were injected into the peritoneal cavity at a different site. The GFP-labeled fibroblast cell line was also injected i.p. on day 14 after the initial transplantation. Animals were killed on day 21. (*c*) Histologic examination of the i.p. tumor generated by Capan-1. The peripheral area of Capan-1 xenografts is characterized by papillary growth. (*d*) Immunofluorescence analysis of GFP-labeled fibroblast cell line (KM104^{GFP}) recruited into cancer stroma. GFP-positive cells (green) were found in the fibrovascular stroma generated by Capan-1 (red). (*e*) Histologic examination of i.p. tumor generated by Capan-1. The central area is characterized by glandular formation surrounded by desmoplastic stroma. (*f*) Immunofluorescence analysis of GFP-labeled fibroblast cell line (KM104^{GFP}) recruited into cancer stroma. GFP-positive cells (green) were found in the desmoplastic stroma generated by Capan-1 (red).

TABLE I – RECRUITMENT OF HFB^{GFP} INTO CANCER STROMA

Cell line	TV (mm^3)	GFP^+ clusters			
		–	+	++	+++
—	55 ± 21	0/7	0/7	0/7	0/7
Bone marrow					
KM101	52 ± 19	4/10	4/10	1/10	1/10
KM102	43 ± 13	4/7	3/7	0/7	0/7
KM103	49 ± 21	3/7	4/7	0/7	0/7
KM104	55 ± 20	0/9	1/9	4/9	4/9
KM105	55 ± 24	4/6	2/6	0/6	0/6
Lung					
IMR-90-SV	26 ± 17*	4/7	3/7	0/7	0/7
MRC-5 SV1 TG1	66 ± 53	1/8	5/8	2/8	0/8
VA-13	94 ± 41*	0/9	0/9	0/9	9/9
Skin					
W-V	76 ± 30	3/8	5/8	0/8	0/8
KM104					
Day 0	61 ± 25	0/7	1/7	2/7	4/7
Day 7	60 ± 15	1/6	2/6	1/6	2/6
Day 14	60 ± 18	1/6	5/6	0/6	0/6
Day 0+14	62 ± 24	0/6	1/6	2/6	3/6

Capan-1 cells and GFP-labeled fibroblast cell lines were injected i.p. at a different site. The same GFP-labeled fibroblast cell lines were also injected i.p. 14 days after the initial transplantation. Control mice received only a Capan-1 injection. Another experiment was performed as follows. Capan-1 cells were injected i.p. on day 0. GFP-labeled KM104 were injected i.p. on day 0, 7 or 14 after the Capan-1 transplantation. The number of GFP^+ clusters was determined on the tumor maximum cut surface. –, 0; +, 1–5; ++, 6–10; +++, ≥11. TV, tumor volume. $^*p < 0.05$.

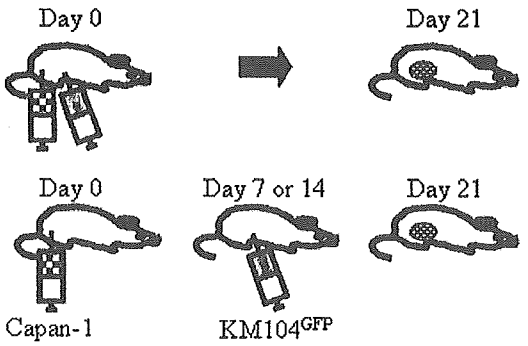

FIGURE 2 – Capan-1 cells (5×10^6/animal) were injected into the peritoneal cavities of SCID mice on day 0. Thereafter, 5×10^6 $KM104^{GFP}$ cells were injected i.p. on day 0, 7 or 14 after Capan-1 transplantation; animals were killed on day 21.

Establishment of KM104 subpopulations with high recruitment efficiency into cancer stroma

GFP-labeled KM104 ($KM104^{GFP}$) and Capan-1 cells were inoculated into the peritoneal cavities of SCID mice. After 21 days, tumors at parapancreatic sites were removed, minced and cultured in 10% FBS RPMI-1640. Under subconfluent conditions, adherent cells were harvested and GFP-positive cells at the same MFI were sorted using the FACScaliber system. After confirming that >90% of each cell line was GFP-positive, the collected GFP-positive KM104 cells were then once again inoculated with Capan-1 into the peritoneal cavities of SCID mice. This procedure was repeated 5 times, and the resulting subpopulation was called $KM104^{GFP}$-5G.

Real-time quantitative PCR analysis

Quantitative PCR was performed using the LightCycler System (Roche Diagnostics, Indianapolis, IN). An aliquot of 4 μg of the extracted total RNA from the tumor mass was reverse-transcribed using ThermoScript and $oligo(dT)_{20}$ as the primer (Invitrogen, La Jolla, CA). The obtained cDNA was diluted 1/10 with water, and 1 μl was used for amplification. PCR was performed with the LightCycler FastStart DNA SYBR Green Kit (Roche Diagnostics), according to the manufacturer's protocol. To control for the specificity of the amplification products, a melting curve analysis was performed. No amplification of nonspecific products was observed. In addition, PCR products were gel-separated to confirm a band of the expected size. The relative initial amount of a particular template in the cDNA mixture was extrapolated from a standard curve. The standards, composed of 5 serial dilutions of one of the cDNAs (ranging from 1×10^8 to 1×10^2 copies/μl), were run in parallel with the samples under identical PCR conditions and amplified using the same set of primers. Using the LightCycler software, the amplification curves of samples were plotted against these standard curves to generate gene-specific mRNA copy numbers. The relative amounts of the resulting products were normalized using the β-actin housekeeping gene. Primer sequences were as follows: β-actin 5′-TTGAAGGTAGTTTCGTGGAT-3′, 5′-GAAAATCTGGCACCACACCTT-3′; GFP 5′-AAGTTCATCTGCACCACCG-3′, 5′-TCCTTGAAGAAGATGGTGCG-3′.

Chemotaxis and chemoinvasion assays

The chemotaxis assay was performed using 24-well culture chambers (Becton Dickinson Labware, Bedford, MA) and a polycarbonate filter with an 8 μm pore size, while the chemoinvasion assay was performed using 24-well culture chambers and a growth factor–reduced, Matrigel-coated filter with a pore size of 8 μm (Becton Dickinson Labware). The lower chamber contained 0.6 ml of RPMI-1640 + 0.1% BSA with Capan-1-released chemoattractant(s) or RPMI-1640 + 0.1% BSA as a control. In the upper compartment, 2×10^4 cells/well were placed in triplicate wells and incubated for 6 hr (chemotaxis assay) or for 24 hr (chemoinvasion assay) at 37°C in a humidified incubator with 5% CO_2. After incubation, the cells that had passed through the filter into the lower wells were stained with hematoxylin and counted under a microscope in 9 predetermined fields.

Microarray analysis

We used human H133A oligonucleotide probe arrays (Affymetrix, Santa Clara, CA) for analysis of mRNA expression levels corresponding to 22,284 transcripts. The procedures were conducted according to the supplier's protocols and are thus described briefly. Total RNA was extracted from cultured $KM104^{GFP}$ and $KM104^{GFP}$-5G by Trizol (Life Technologies, Bethesda, MD) reagent. Every 1 mg of total RNA was used to generate a cRNA probe by T7 transcription. Fragmented cRNA (10 mg) was hybridized to the microarrays in 200 ml of a hybridization cocktail at

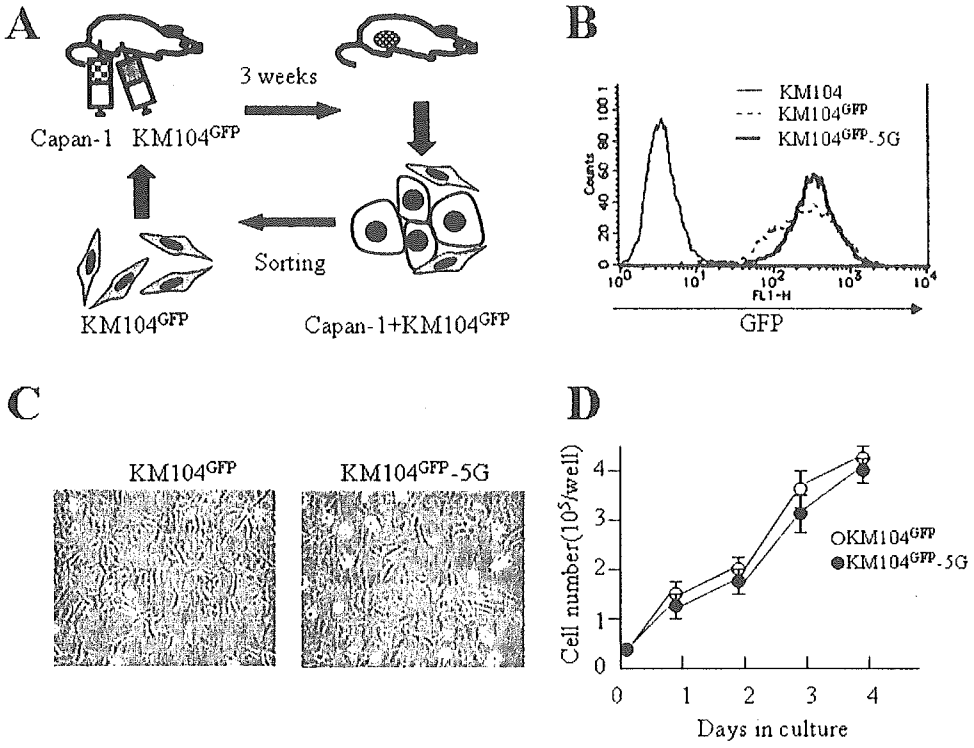

FIGURE 3 – Establishment of KM104^{GFP} subpopulations with higher recruitment efficiency into cancer stroma. (*a*) Schematic representation of the *in vivo* selection of KM104^{GFP}. KM104^{GFP} was inoculated into the peritoneal cavities of SCID mice with Capan-1 xenografts. After 21 days, the tumor was removed, minced and cultured. Under subconfluent conditions, adherent cells were harvested and the GFP-positive cells sorted. The collected GFP-positive KM104 cells were then repeatedly inoculated into peritoneal cavities with Capan-1. (*b*) FACS analysis of KM104^{GFP} and KM104^{GFP}-5G after *in vivo* selection. (*c*) Morphologic appearance of KM104^{GFP} and KM104^{GFP}-5G *in vitro*. (*d*) Growth of KM104^{GFP} and KM104^{GFP}-5G in monolayer culture. KM104^{GFP} and KM104^{GFP}-5G cells were seeded at 5×10^4/well on day 0 and the number of cells per well was determined on days 1, 2, 3 and 4.

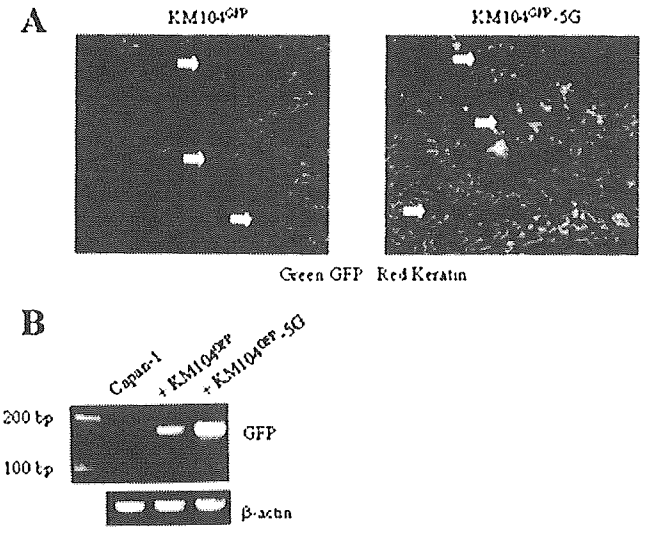

FIGURE 4 – KM104^{GFP}-5G exhibited higher recruitment efficiency than KM104^{GFP}. (*a*) Immunofluorescence analysis of KM104^{GFP} and KM104^{GFP}-5G recruited into cancer stroma. (*Left*) KM104^{GFP} cells were found scattered throughout the stroma (arrows). (*Right*) Numerous KM104^{GFP}-5G cells were found in the stroma (arrows). (*b*) Quantitative PCR analysis of GFP expression in the resected peritoneal tumor. GFP-specific primers amplified a band of 173 bp.

45°C for 16 hr in a rotisserie oven set at 60 rpm. The arrays were then washed with nonstringent wash buffer (6 × SSPE) at 25°C followed by stringent wash buffer [100 mM MES (pH6.7), 0.1 M NaCl and 0.01% Tween-20] at 50°C, stained with streptavidin phycoerythrin (Molecular Probes), washed again with 6 × SSPE, stained with biotinylated antistreptavidin IgG followed by a second staining with streptavidin phycoerythrin and washed a third time with 6 × SSPE. The arrays were scanned using the Gene Array scanner (Affymetrix) at 3 μm resolution, and the scanned image was quantitatively analyzed with Microarray Suite 5.0 software (Affymetrix). For normalizing the data to compare mRNA expression levels among samples, we unified 1,000 as an average of average difference (AD) scores corresponding to signal intensities of all probe sets in each sample. For statistical analysis to select genes, Microsoft Excel (Redmond, WA) was used. Each experiment was done in duplicate. Duplicate experiments were conducted completely independently of each other.

RESULTS

In vivo *model for recruitment of human fibroblast cell lines into xenotransplanted cancer stroma*

Nine human fibroblast cell lines from bone marrow, lung and skin were genetically modified by GFP retroviral transfection; and the GFP-positive cells were sorted. After confirming that >90% of each cell line was GFP-positive (hFB^{GFP}), they were used in the following experiment (Fig. 1*a*). The human pancreatic cancer cell line Capan-1 was inoculated i.p. into SCID mice, and hFB^{GFP} cells were administered according to the schedule outlined in Figure 1*b*. By day 21, all Capan-1 cells had formed tumor masses in the peritoneum at the injection site, parapancreas and hilum of the spleen and liver. Although tumor sizes varied among cases, the tumor in the parapancreas region was the largest in each animal. The peripheral area of the Capan-1 xenografts at the parapancreas site was characterized by papillary growth (Fig. 1*c*), while the central area exhibited a glandular formation surrounded by desmoplastic stroma (Fig. 1*e*). Immunofluorescence examination, enhanced using a GFP antibody, revealed the presence of hFB^{GFP} within both the papillary stroma (Fig. 1*d*) and the desmoplastic stroma (Fig. 1*f*). We examined the presence of hFB^{GFP} in the intestine, liver and spleen by immunohistochemical analysis but did not find any GFP-positive cells. Furthermore, none of the 9 fibroblast cell lines induced metastatic spread of Capan-1 into other organs (data not shown). Table I shows the recruitment efficiency of hFB^{GFP} into the cancer stroma. Although hFB^{GFP} originating from bone marrow did not affect tumor growth, 8 of 9 KM104^{GFP} showed moderate (++) or high (+++) recruitment efficiency. On the contrary, when KM102^{GFP}, 103^{GFP} and 105^{GFP} were injected with Capan-1, the number of

TABLE II – RECRUITMENT OF KM104^{GFP} AND KM104^{GFP}-5G INTO CANCER STROMA

Cell line	TV (mm^3)	GFP$^+$ clusters			
		–	+	++	+++
KM104^{GFP}	61 ± 25	0/7	1/7	2/7	4/7
KM104^{GFP}-5G	65 ± 31	0/7	0/7	0/7	7/7

Capan-1 cells were injected i.p. on day 0. After 1 hr, KM104^{GFP} and KM104^{GFP}-5G were injected i.p. at a different site. The number of GFP$^+$ clusters was determined on the tumor maximum cut surface. –, 0; +, 1–5; ++, 5–10; +++, ≥11. TV, tumor volume.

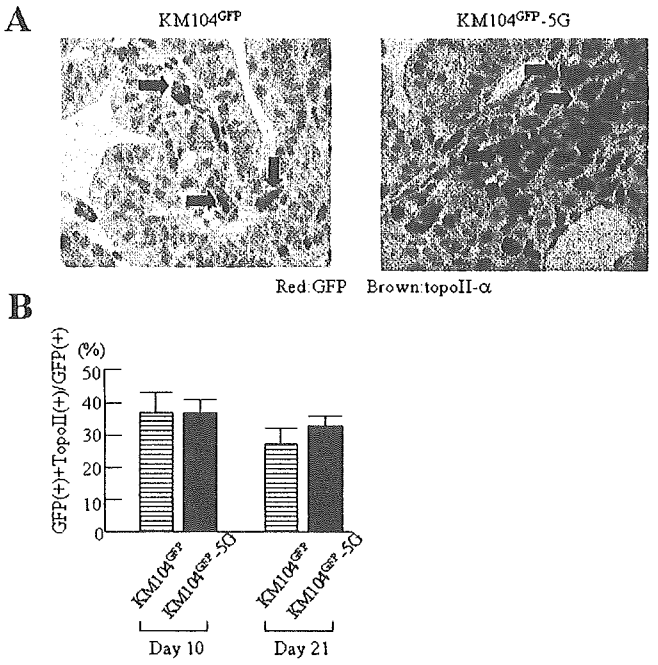

FIGURE 5 – Proliferative activity of KM104^{GFP} and KM104^{GFP}-5G within cancer stroma on days 10 and 21. (*a*) Double immunolabeling of topoisomerase IIα and GFP (day 21). Nuclear positive staining for topoisomerase IIα appears as brown, while cytoplasmic positive staining for GFP appears as red. Arrows indicate both topoisomerase IIα- and GFP-positive cells. (*b*) Ratio of topoisomerase IIα-positive cells to GFP-positive cells on days 10 and 21.

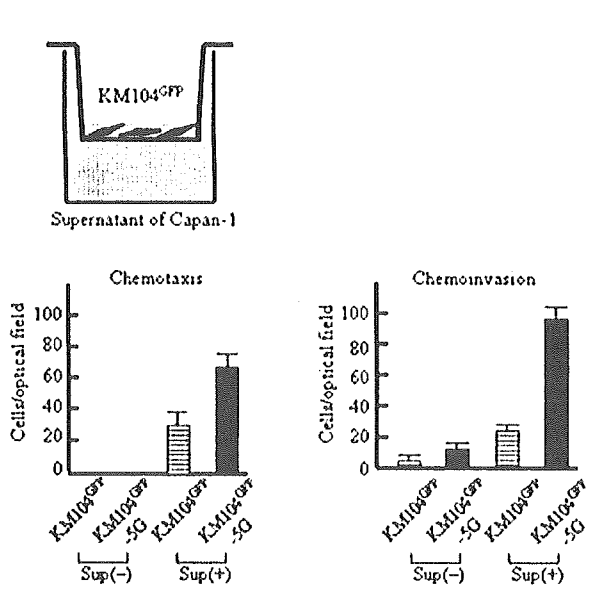

FIGURE 6 – KM104^{GFP}-5G exhibited higher chemotaxis and chemoinvasion capacity than KM104^{GFP}. (*a*) Schematic representation of the chemotaxis and chemoinvasion assays: the lower chamber contained 0.6 ml of RPMI-1640 + 0.1% BSA with Capan-1-released chemoattractant(s) or RPMI-1640 + 0.1% BSA as a control. Next, 2×10^4 KM104^{GFP} or KM104^{GFP}-5G cells were placed in the upper compartment and incubated for 6 hr (chemotaxis assay) and for 24 hr (chemoinvasion assay). Cells that migrated through the porous membrane were stained and counted. Cells were counted in microscopic fields at ×200 magnification. Nine fields were selected for cell counting, and each numerical value was averaged. (*b*) Number of cells that passed through the filter into the lower wells in response to the Capan-1-released chemoattractant(s).

cases with GFP-positive clusters was lower than when KM104^{GFP} was injected. hFB^{GFP} originating from lung exhibited variable recruitment efficiency. VA-13^{GFP} promoted tumor growth by about 2-fold and showed the highest recruitment efficiency. However, IMR-90-SV^{GFP} reduced the tumor volume by half, and its recruitment efficiency was low. The recruitment efficiencies of MRC-5 SV1 TG1^{GFP} from lung and W-V^{GFP} from skin were intermediate and low, respectively.

Early-phase interactions between KM104^{GFP} and Capan-1 are required for efficient recruitment into cancer stroma

To investigate when the cellular interactions between hFB^{GFP} and Capan-1 that are responsible for efficient recruitment into the cancer stroma occur, we inoculated KM104^{GFP} on day 0, 7 or 14 (Fig. 2). KM104^{GFP} was used for this experiment since this cell line did not affect tumor volume, unlike VA-13^{GFP} (Table I). As expected, the tumor volume was not influenced by this injection protocol. When KM104^{GFP} was administered on day 0, 6 of 7 (85.7%) showed moderate (++) or high (+++) recruitment efficiency, which was almost the same as on both day 0 and day 14 injection (5/6, 83.3%; Table I). However, when KM104^{GFP} was administered on day 14, the recruitment efficiency decreased and no case showed moderate or high recruitment efficiency. These results suggest that early cellular interactions between Capan-1 and KM104^{GFP} are required for efficient recruitment into cancer stroma.

In vivo *selection of a KM104^{GFP} subpopulation with a higher recruitment efficiency in Capan-1-induced stroma*

To establish a KM104^{GFP} subpopulation with higher recruitment efficiency, we performed 5 cyclic *in vivo* selections of KM104^{GFP} in Capan-1-induced stroma, as shown in Figure 3*a* (KM104^{GFP}-5G). The population of GFP-positive cells in KM104^{GFP} and KM104^{GFP}-5G was 95.0% and 96.7%, respectively; and MFI of GFP in KM104^{GFP} and KM104^{GFP}-5G was 339 and 380, respectively (Fig. 3*b*). Morphologically, KM104^{GFP}-5G exhibited a spindle shape that was similar to KM104^{GFP} (Fig. 3*c*). Growth of KM104^{GFP} and KM104^{GFP}-5G cells in monolayer culture did not significantly differ, indicating that there is no critical difference in proliferative activity or other growth-determining cellular features of these fibroblast subclones (Fig. 3*d*). When Capan-1 was injected with KM104^{GFP}-5G, numerous GFP-positive clusters were found within cancer stroma (Fig. 4*a*). In KM104^{GFP}, 4/7 showed high (+++) and 2/7 showed moderate (++) recruitment efficiency, whereas all cases (7/7) showed high (+++) recruitment efficiency in KM104^{GFP}-5G (Table II), indicating higher recruitment efficiency in KM104^{GFP}-5G. Quantitative RT-PCR analysis revealed that the relative copy numbers of GFP/β-actin (10^{-2}) in tumor masses injected with KM104^{GFP}-5G and in those injected with KM104^{GFP} were 115.8 and 13.8, respectively (Fig. 4*b*). We double immunostained the cells with GFP and topoisomerase IIα, whose expression is limited mostly to the S-to-G_2/M phases of the cell cycle[22] (Fig. 5*a*). The topoisomerase IIα-positive cell ratios for GFP-positive KM104^{GFP} and KM104^{GFP}-

TABLE III – CDNA MICROARRAY SEARCH FOR GENES THAT ARE >3-FOLD DIFFERENTIALLY EXPRESSED IN KM104^{GFP}-5G

Genebank	Gene name	Fold change
Genes upregulated in KM104^{GFP}-5G		
NM002273	Keratin-8	6.0
NM004415	Desmoplakin	5.6
NM003543	Zing finger protein 198	3.8
NM005682	G protein–coupled receptor 56	3.7
NM001216	CA IX	3.0
NM004436	Endosulfine-α	3.0
NM005901	Mothers against decapentaplegic homolog 2	3.0
NM002345	Lumican	3.0
Genes downregulated in KM104^{GFP}-5G		
NM014459	Protocadherin-17	0.1
NM012453	Transducin β-like 20	0.2
NM001004	Ribosomal protein, large P2	0.2
NM005195	CCAAT/enhancer binding protein δ	0.2
XM168302	Zinc finger protein 36	0.3
NM004436	Hypothetical protein FLJ20375	0.3

5G cells on day 10 xenografts were 37.0 ± 7.3% and 37.1 ± 5.4%, respectively, and those on day 21 xenografts were 27.4 ± 4.5% and 32.9 ± 3.7%, respectively; these differences were not significant (Fig. 5*b*). These results indicated that higher recruitment efficiency of KM104^{GFP}-5G was not caused by increased proliferative activity.

KM104^{GFP}-5G exhibited higher chemotaxis and chemoinvasion activity

Fibroblast recruitment is thought to involve several sequential events, such as migration, proliferation and survival within the cancer microenvironment. We therefore examined whether KM104^{GFP} and KM104^{GFP}-5G exhibited any differences in chemotaxis or chemoinvasion activity. When KM104^{GFP} and KM104^{GFP}-5G were placed on transwell chambers, the number of migrating cells increased in response to Capan-1-released chemoattractant(s); however, KM104^{GFP}-5G exhibited a 2.4-fold higher migratory capacity than KM104^{GFP} (KM104^{GFP} 28.1 ± 6.0/field *vs.* KM104^{GFP}-5G 68.0 ± 1.6/field). When KM104^{GFP} and KM104^{GFP}-5G were placed on a Matrigel transwell chamber, the invasion capacity of KM104^{GFP}-5G was 3.1-fold higher than that of KM104^{GFP} (KM104^{GFP} 4.1 ± 1.1/field *vs.* KM104^{GFP}-5G 12.6 ± 4.6/field) without any chemoattractants and 4.3-fold higher (KM104^{GFP} 22.3 ± 2.9/field *vs.* KM104^{GFP}-5G 95.5 ± 10.2/field) in response to Capan-1-released chemoattractant(s) (Fig. 6).

Comparison of expression profiles between KM104^{GFP} and KM104^{GFP}-5G

To identify the genes differently expressed in KM104^{GFP}-5G, genomewide screening for genes with different expression patterns in KM104^{GFP} and KM104^{GFP}-5G was performed using a microarray containing 22,284 probes. We performed duplicate microarray analysis and selected the genes with >3-fold up- or downregulation in both experiments. Eight genes with >3-fold upregulation and 6 genes with >3-fold downregulation in KM104^{GFP}-5G were identified (Table III). The upregulated genes were keratin-8 and desmolakin (microfilaments and cytoskeleton), zinc finger protein 198 (transcription and translation), G protein–coupled receptor 56 and CA IX (membrane proteins), mothers against decapentaplegic homolog 2 (signal transduction), lumican (cell–matrix interactions) and endosulfine-α (others). The downregulated genes were protocadherin-17 (cell–matrix interactions), ribosomal protein large P2, CCAAT/enhancer binding protein δ and zinc finger protein-36 (transcription and translation) as well as transducin (beta)-like 20 and hypothetical protein FLJ20375 (others). Significant differences in the expression of genes directly involved in cell migration and/or invasion (MMP family) were not found in KM104^{GFP}-5G.

TABLE IV – EXPRESSION PROFILES FOR CA IX AND KERATIN-8 IN hFB^{GFP}

Cell line	CA IX	Keratin-8
Bone marrow		
KM101	25.4	5.4
KM102	6.8	3.1
KM103	1.2	2.2
KM104	5.1	27.0
KM104-5G	28.4	37.2
KM105	0.5	6.0
Lung		
IMR-90-SV	2.4	1.7
MRC-5 SV1 TG1	0.5	19.9
VA-13	20.6	6.4
Skin		
W-V	0.0	7.3

Total RNA was extracted from 9 GFP-labeled fibroblast cell lines and KM104^{GFP}-5G, and quantitative RT-PCR was performed. The relative amounts of the resulting products were normalized using β-actin.

Immunohistochemical staining of CA IX and keratin-8 in fibroblasts in pancreatic ductal cancers

To verify whether expression of the genes identified in microarray experiments could be found in the recruited fibroblasts within cancer stroma, we selected 2 genes (CA IX and keratin-8). The results obtained by microarray were confirmed by real-time quantitative PCR. Relative amounts of transcription for CA IX and keratin-8 in 9 fibroblast cell lines and KM104^{GFP}-5G are summarized in Table IV. Transcripts for CA IX and keratin-8 in KM104^{GFP}-5G were 5.6-fold and 1.4-fold higher, respectively, than in KM104^{GFP}. Then, their protein expression was immunohistochemically analyzed in xenografts and surgically resected pancreatic cancers. In the xenografts, KM104^{GFP} recruited into Capan-1-induced stroma expressed CA IX (Fig. 7*a,b*) but not keratin-8 (data not shown). Overexpression of CA IX was observed in fibroblasts within pancreatic cancer stroma, with desmoplastic reaction in 6 of 8 cases (Fig. 7*c*). On the contrary, its expression was weak or under the detection level in fibroblasts within noncancerous pancreatic tissue (Fig. 7*d*). Overexpression of keratin-8 in fibroblasts within cancer stroma was observed in 2 of 8 cases (Fig. 7*e*), whereas its expression in fibroblasts was under the detection level in noncancerous pancreatic tissue (Fig. 7*f*).

Discussion

During cancer invasion, fibroblasts as well as inflammatory cells are recruited into cancer-induced stroma in response to chemotactic signals produced by the cancer cells. One of the first demonstrations of recruitment of genetically modified endothelial cells showed that rat brain endothelial cells can stably engraft into glioma-associated vessels.[23] Recently reported evidence has shown that exogenously administered human endothelial cells and fibroblasts are selectively recruited into the microvasculature and stromal compartment, respectively, of human tumors growing i.p. in SCID mice.[11] We also demonstrated in the present study that GFP-labeled human fibroblast cell lines were incorporated into cancer stroma. Furthermore, KM104^{GFP} (from bone marrow) and VA-13^{GFP} (from lung) were recruited more efficiently than the other cell lines. These results indicate that the recruitment of fibroblasts into cancer stroma is regulated by the properties of the fibroblasts themselves, which appears to agree with the results of previous *in vitro* studies showing that fibroblasts within cancer stroma and normal tissue are phenotypically and functionally distinct.[24–27]

Interestingly, although KM104^{GFP} was efficiently recruited, it did not influence tumor growth. However, VA-13^{GFP} was efficiently recruited and promoted tumor growth. The integration of fibroblasts in the tumor mass would not contribute to the increase

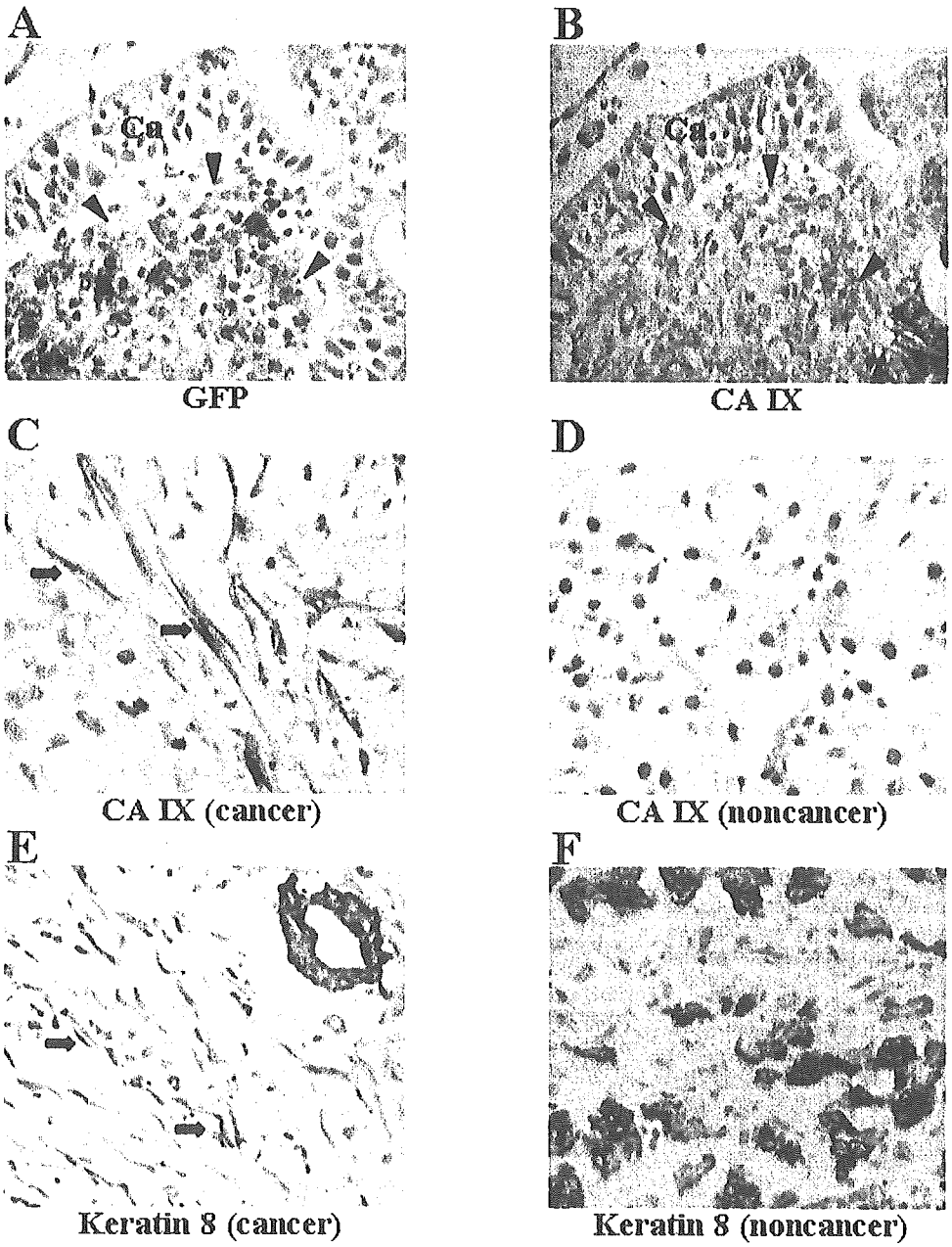

FIGURE 7 – Recruited fibroblasts into cancer stroma expressed CA IX and keratin-8. (*a*) KM104^{GFP} recruited into Capan-1 induced stroma. Section was stained with GFP. Arrowheads indicate the cluster of KM104^{GFP}. (*b*) Serial section was stained with CA IX. Note KM104^{GFP} showing CA IX-positive. Parts of Capan-1 also were positive for CA IX. (*c*) Recruited fibroblasts (arrows) in invasive pancreatic cancer with desmoplastic stroma showed strongly positive reaction for CA IX. (*d*) Fibroblasts within noncancerous pancreatic tissue showed weak or negative staining for CA IX. (*e*) Recruited fibroblasts (arrows) in invasive pancreatic cancer showed positive reaction for keratin-8. (*f*) Fibroblasts within noncancerous pancreatic tissue showed negative staining for keratin-8, whereas exocrine glands were strongly positive for keratin-8.

of tumor volume since the number of recruited fibroblasts was <5% in the resected tumor by microscopic analysis. In addition, IMR-90-SV^{GFP} reduced tumor growth significantly, while W-V^{GFP}, which showed similar recruitment efficiency as IMR-90-SV^{GFP}, promoted tumor growth. Therefore, the biologic characteristics of fibroblasts could influence not only the recruitment efficiency of fibroblasts themselves but the growth of cancer cells. We are now investigating the mechanism by which recruited VA-13 promotes xenograft volume. We used KM104^{GFP}, which exhibited high recruitment efficiency but did not affect tumor growth, in the following studies.

When KM104^{GFP} cells were administered on day 14, the recruitment efficiency was obviously lower than when they were administered on day 0. We previously reported that most myofibroblasts within cancer stroma at the early phase of cancer progression were of residual tissue origin, whereas at the late phase, 40% of myofibroblasts were of bone marrow origin.[12] These findings imply that the cancer microenvironment at the late phase provides an optimal condition for the recruitment of fibroblasts from the peripheral blood, rather than from the local connective tissue around the cancer nests. As tumor microenvironments of early and late phases might recruit different kinds of fibroblast, we speculate that early phase, but not late phase, Capan-1-induced microenvironment was suitable for the recruitment of KM104^{GFP}.

Fibroblasts within cancer stroma are biologically heterogeneous, and this heterogeneity has many ramifications for studies on tumor biology.[28–34] To select and maintain fibroblast variants with a higher recruitment potential from a heterogeneous population, we performed *in vivo* selection[35] using the KM104^{GFP} cell line. After 5 cyclic *in vivo* selections within cancer stroma, we obtained a subpopulation with an 8.4-fold higher recruitment potential (KM104^{GFP}-5G). We investigated whether the higher recruitment of KM104^{GFP}-5G *in vivo* is functionally linked with its migration and invasion capacity *in vitro*. Although both KM104^{GFP} and

KM104^{GFP}-5G exhibited migratory potential in response to Capan-1-released chemoattractant(s), KM104^{GFP}-5G had higher migratory activity. Most interestingly, when KM104^{GFP} and KM104^{GFP}-5G were subjected to a Matrigel invasion assay, KM104^{GFP}-5G also exhibited a higher degree of invasiveness. Several reports have described fibroblasts from pathogenic fibrotic lesions, including cancer tissue, exhibiting "transformed" behavior.[15,36–39] Fibroblast-like synoviocytes derived from rheumatoid arthritis joints were highly invasive and have functional implications for the matrix degradation of cartilage, whereas cells from normal tissues were not invasive.[38] Based on these findings, one may postulate that fibroblasts within cancer stroma have a migratory and invasive capacity similar to that of cancer cells and associate with cancer cells by transmitting reciprocal signals. This hypothesis is also supported by the fact that exogenous KM104^{GFP} administered on day 0 was found in both central and peripheral areas of the cancer tissue on day 21 (Fig. 1*c–f*).

Considering the results obtained from the oligonucleotide microarray method, we have focused on CA IX and keratin-8, which were significantly upregulated in KM104^{GFP}-5G. Their protein expression was actually upregulated in recruited fibroblasts within cancer stroma of invasive pancreatic cancer cases. CA IX is a novel member of the carbonic anhydrase family that codes for a transmembrane glycoprotein with an extracellular catalytic domain; its expression is strongly induced by hypoxia.[40,41] Colpaert et al.[42] reported that CA IX expression was found in not only breast cancer cells but also fibroblasts within the cancer stroma and that expression in fibroblasts was associated with poor prognosis. Keratin-8, an intermediate filament, is mainly expressed in epithelial cells but is also found in human decidual stromal cells, embryonal mesenchymal cells and SV-40 transformed fibroblasts *in vitro*.[43,44] Moreover, forced expression of keratins 8 and 18 in mouse L cells augmented cell migration and invasion.[45] Nakagawa *et al.*[46] analyzed molecular expression profiles of cancer-associated fibroblasts in colon cancer metastasis and indicated that these fibroblasts form a favorable microenvironment for cancer cells. According to their results, genes upregulated in cancer-associated fibroblasts compared to skin fibroblasts included keratin-18, which is not found in normal stromal cells. Taking these observation and our results into consideration, keratin upregulation in fibroblasts may be a key phenomenon for the recruitment into cancer-induced stroma. Further research should address the precise role of these genes with regard to fibroblast recruitment in our model using gene overexpression or silencing methods, although the possible effects of posttranscriptional modifications must be kept in mind.

By targeting the tumor microenvironment, treatment effectiveness could be increased.[47,48] Much work on the biologic mechanisms of fibroblast recruitment is needed, but the present results suggest that fibroblasts could be used as a biologic tracer of cancer cells and could act as an efficient drug delivery system to prevent or slow the local growth of cancer cells.

Acknowledgements

We are grateful to Dr. T. Kitamura (Institute of Medical Science, University of Tokyo, Tokyo, Japan) for providing the retroviral plasmid pMX-GFP. We also thank Ms. C. Okumura and Ms. Y. Okuhara for technical support as well as Ms. M. Suzaki for preparing the manuscript.

References

1. Plate JM, Harris JE. Immune cell functions in pancreatic cancer. Crit Rev Immunol 2000;20:375–92.
2. Herberman RB. Cancer immunotherapy with natural killer cells. Semin Oncol 2002;29:27–30.
3. Coussens LM, Werb Z. Inflammation and cancer. Nature 2002;420: 860–7.
4. Smyth MJ, Crowe NY, Hayakawa Y, Takeda K, Yagita H, Godfrey DI. NKT cells—conductors of tumor immunity? Curr Opin Immunol 2002;14:165–71.
5. Folkman J, Hahnfeldt P, Hlatky L. Cancer: looking outside the genome. Nat Rev Mol Cell Biol 2000;1:76–9.
6. Carmeliet P, Jain RK. Angiogenesis in cancer and other diseases. Nature 2000;14:249–57.
7. Elenbaas B, Weinberg RA. Heterotypic signaling between epithelial tumor cells and fibroblasts in carcinoma formation. Exp Cell Res 2001;264:169–84.
8. Kunz-Schughart LA, Knuechel R. Tumor-associated fibroblasts (part I): active stromal participants in tumor development and progression? Histol Histopathol 2002;17:599–621.
9. Kunz-Schughart LA, Knuechel R. Tumor-associated fibroblasts (part II): functional impact on tumor tissue. Histol Histopathol 2002;17:623–37.
10. Studeny M, Marini FC, Champlin RE, Zompetta C, Fidler IJ, Andreeff M. Bone marrow–derived mesenchymal stem cells as vehicles for interferon-beta delivery into tumors. Cancer Res 2002;62: 3603–8.
11. Roni V, Habeler W, Parenti A, Indraccolo S, Gola E, Tosello V, Cortivo R, Abatangelo G, Chieco-Bianchi L, Amadori A. Recruitment of human umbilical vein endothelial cells and human primary fibroblasts into experimental tumors growing in SCID mice. Exp Cell Res 2003;287:28–38.
12. Ishii G, Sangai T, Oda T, Aoyagi Y, Hasebe T, Kanomata N, Endoh Y, Okumura C, Okuhara Y, Magae J, Emura M, Ochiya T, Ochiai A. Bone-marrow-derived myofibroblasts contribute to the cancer-induced stromal reaction. Biochem Biophys Res Commun 2003;309: 232–40.
13. Direkze NC, Hodivala-Dilke K, Jeffery R, Hunt T, Poulsom R, Oukrif D, Alison MR, Wright NA. Bone marrow contribution to tumor-associated myofibroblasts and fibroblasts. Cancer Res 2004;64:8492–5.
14. Barcellos-Hoff MH, Ravani SA. Irradiated mammary gland stroma promotes the expression of tumorigenic potential by unirradiated epithelial cells. Cancer Res 2000;60:1254–60.
15. Tlsty TD. Stromal cells can contribute oncogenic signals. Semin Cancer Biol 2001;11:97–104.
16. Hasebe T, Sasaki S, Imoto S, Ochiai A. Proliferative activity of intratumoral fibroblasts is closely correlated with lymph node and distant organ metastases of invasive ductal carcinoma of the breast. Am J Pathol 2000;156:1701–10.
17. Hasebe T, Sasaki S, Imoto S, Ochiai A. Highly proliferative fibroblasts forming fibrotic focus govern metastasis of invasive ductal carcinoma of the breast. Mod Pathol 2001;14:325–37.
18. Hasebe T, Imoto S, Ogura T, Mukai K. Significance of basic fibroblast growth factor and fibroblast growth factor receptor protein expression in the formation of fibrotic focus in invasive ductal carcinoma of the breast. Jpn J Cancer Res 1997;88:877–85.
19. Okusa Y, Ichikura T, Mochizuki H. Prognostic impact of stromal cell–derived urokinase-type plasminogen activator in gastric carcinoma. Cancer 1999;85:1033–8.
20. Harigaya K, Handa H. Generation of functional clonal cell lines from human bone marrow stroma. Proc Natl Acad Sci USA 1985;82:3477–80.
21. Kitamura T, Koshino Y, Shibata F, Oki T, Nakajima H, Nosaka T, Kumagai H. Retrovirus-mediated gene transfer and expression cloning: powerful tools in functional genomics. Exp Hematol 2003;11: 1007–14.
22. Ito K, Sasano H, Yabuki N, Matsunaga G, Sato S, Kikuchi A, Yajima A, Nagura H. Immunohistochemical study of Ki-67 and DNA topoisomerase II in human endometrium. Mod Pathol 1997; 10:289–94.
23. Lal B, Indurti RR, Couraud PO, Goldstein GW, Laterra J. Endothelial cell implantation and survival within experimental gliomas. Proc Natl Acad Sci USA 1994;91:9695–9.
24. Jacoby RF, Schlack S, Cole CE, Skarbek M, Harris C, Meisner LF. A juvenile polyposis tumor suppressor locus at 10q22 is deleted from nonepithelial cells in the lamina propria. Gastroenterology 1997; 112:1398–1403.
25. Moinfar F, Man YG, Arnould L, Bratthauer GL, Ratschek M, Tavassoli FA. Concurrent and independent genetic alterations in the stromal and epithelial cells of mammary carcinoma: implications for tumorigenesis. Cancer Res 2000;60:2562–6.
26. Tuxhorn JA, McAlhany SJ, Dang TD, Ayala GE, Rowley DR. Stromal cells promote angiogenesis and growth of human prostate tumors in a differential reactive stroma (DRS) xenograft model. Cancer Res 2002;62:3298–307.
27. Walter-Yohrling J, Pratt BM, Ledbetter S, Teicher BA. Myofibroblasts enable invasion of endothelial cells into three-dimensional tumor cell clusters: a novel in vitro tumor model. Cancer Chemother Pharmacol 2003;52:263–9.

28. Garrett DM, Conrad GW. Fibroblast-like cells from embryonic chick cornea, heart, and skin are antigenically distinct. Dev Biol 1979;70: 50–70.
29. Schor SL, Schor AM. Clonal heterogeneity in fibroblast phenotype: implications for the control of epithelial–mesenchymal interactions. Bioessays 1987;7:200–4.
30. Alvarez RJ, Sun MJ, Haverty TP, Iozzo RV, Myers JC, Neilson EG. Biosynthetic and proliferative characteristics of tubulointerstitial fibroblasts probed with paracrine cytokines. Kidney Int 1992;41:14–23.
31. Ronnov-Jessen L, Van Deurs B, Nielsen M, Petersen OW. Identification, paracrine generation, and possible function of human breast carcinoma myofibroblasts in culture. In Vitro Cell Dev Biol 1992; 28A:273–83.
32. Dugina V, Alexandrova A, Chaponnier C, Vasiliev J, Gabbiani G. Rat fibroblasts cultured from various organs exhibit differences in alpha-smooth muscle actin expression, cytoskeletal pattern, and adhesive structure organization. Exp Cell Res 1998;238:481–90.
33. Jelaska A, Strehlow D, Korn JH. Fibroblast heterogeneity in physiological conditions and fibrotic disease. Springer Semin Immunopathol 1999;21:385–95.
34. Petersen OW, Nielsen HL, Gudjonsson T, Villadsen R, Rank F, Niebuhr E, Bissell MJ, Ronnov-Jessen L. Epithelial to mesenchymal transition in human breast cancer can provide a nonmalignant stroma. Am J Pathol 2003;162:391–402.
35. Fidler IJ. Selection of successive tumour lines for metastasis. Nat New Biol 1973;242:148–9.
36. Muller-Ladner U, Kriegsmann J, Franklin BN, Matsumoto S, Geiler T, Gay RE, Gay S. Synovial fibroblasts of patients with rheumatoid arthritis attach to and invade normal human cartilage when engrafted into SCID mice. Am J Pathol 1996;149:1607–15.
37. Roivainen A, Soderstrom KO, Pirila L, Aro H, Kortekangas P, Merilahti-Palo R, li-Jama TY, Toivanen A, Toivanen P. Oncoprotein expression in human synovial tissue: an immunohistochemical study of different types of arthritis. Br J Rheumatol 1996;35:933–42.
38. Wibulswas A, Croft D, Pitsillides AA, Bacarese-Hamilton I, McIntyre P, Genot E, Kramer IM. Influence of epitopes CD44v3 and CD44v6 in the invasive behavior of fibroblast-like synoviocytes derived from rheumatoid arthritic joints. Arthritis Rheum 2002;46:2059–64.
39. Seemayer CA, Kuchen S, Kuenzler P, Rihoskova V, Rethage J, Aicher WK, Michel BA, Gay RE, Kyburz D, Neidhart M, Gay S. Cartilage destruction mediated by synovial fibroblasts does not depend on proliferation in rheumatoid arthritis. Am J Pathol 2003;162:1549–57.
40. Wykoff CC, Beasley N, Watson PH, Campo L, Chia SK, English R, Pastorek J, Sly WS, Ratcliffe P, Harris AL. Expression of the hypoxia-inducible and tumor-associated carbonic anhydrases in ductal carcinoma in situ of the breast. Am J Pathol 2001;158:1011–19.
41. Potter CP, Harris AL. Diagnostic, prognostic and therapeutic implications of carbonic anhydrases in cancer. Br J Cancer 2003;89:2–7.
42. Colpaert CG, Vermeulen PB, Fox SB, Harris AL, Dirix LY, Van Marck EA. The presence of a fibrotic focus in invasive breast carcinoma correlates with the expression of carbonic anhydrase IX and is a marker of hypoxia and poor prognosis. Breast Cancer Res Treat 2003;81:137–47.
43. von Koskull H, Virtanen I. Induction of cytokeratin expression in human mesenchymal cells. J Cell Physiol 1987;133:321–9.
44. Knapp AC, Bosch FX, Hergt M, Kuhn C, Winter-Simanowski S, Schmid E, Regauer S, Bartek J, Franke WW. Cytokeratins and cytokeratin filaments in subpopulations of cultured human and rodent cells of nonepithelial origin: modes and patterns of formation. Differentiation 1989;42:81–102.
45. Chu YW, Runyan RB, Oshima RG, Hendrix MJ. Expression of complete keratin filaments in mouse L cells augments cell migration and invasion. Proc Natl Acad Sci USA 1993;90:4261–5.
46. Nakagawa H, Liyanarachchi S, Davuluri RV, Auer H, Martin EW Jr, de la Chapelle A, Frankel WL. Role of cancer-associated stromal fibroblasts in metastatic colon cancer to the liver and their expression profiles. Oncogene 2004;23:7366–77.
47. Bissell MJ, Radisky D. Putting tumours in context. Nature Rev Cancer 2001;1:46–54.
48. Cheng JD, Weiner LM. Tumors and their microenvironments: tilling the soil. Clin Cancer Res 2003;9:1590–5.

balt2/zmk-mbc/zmk-mbc/zmk00206/zmk7520-06a | eideg | S=4 | 12/28/05 | 9:30 | Art: | Input-cip

Molecular Biology of the Cell
Vol. 17, 000–000, February 2006

MAGI-1 Is Required for Rap1 Activation upon Cell–Cell Contact and for Enhancement of Vascular Endothelial Cadherin-mediated Cell Adhesion[D] [V]

Atsuko Sakurai, Shigetomo Fukuhara, Akiko Yamagishi, Keisuke Sako, Yuji Kamioka, Michitaka Masuda, Yoshikazu Nakaoka, and Naoki Mochizuki

Department of Structural Analysis, National Cardiovascular Center Research Institute, Suita, Osaka 565-8565, Japan

Submitted July 19, 2005; Revised November 28, 2005; Accepted November 29, 2005
Monitoring Editor: Martin A. Schwartz

Rap1 is a small GTPase that regulates adherens junction maturation. It remains elusive how Rap1 is activated upon cell–cell contact. We demonstrate for the first time that Rap1 is activated upon homophilic engagement of vascular endothelial cadherin (VE-cadherin) at the cell–cell contacts in living cells and that MAGI-1 is required for VE-cadherin-dependent Rap1 activation. We found that MAGI-1 localized to cell–cell contacts presumably by associating with β-catenin and that MAGI-1 bound to a guanine nucleotide exchange factor for Rap1, PDZ-GEF1. Depletion of MAGI-1 suppressed the cell–cell contact-induced Rap1 activation and the VE-cadherin-mediated cell–cell adhesion after Ca^{2+} switch. In addition, relocation of vinculin from cell–extracellular matrix contacts to cell–cell contacts after the Ca^{2+} switch was inhibited in MAGI-1-depleted cells. Furthermore, inactivation of Rap1 by overexpression of Rap1GAPII impaired the VE-cadherin-dependent cell adhesion. Collectively, MAGI-1 is important for VE-cadherin-dependent Rap1 activation upon cell–cell contact. In addition, once activated, Rap1 upon cell–cell contacts positively regulate the adherens junction formation by relocating vinculin that supports VE-cadherin-based cell adhesion.

AQ: A

INTRODUCTION

Intercellular adhesion of vascular endothelial cells is essential for connecting neighboring endothelial cells to develop a vascular tree and to function as a barrier separating blood and tissues. Vascular endothelial cell adhesion is characterized by the overlapping of adherens junctions (AJs) and tight junctions (TJs). AJs are constituted by vascular endothelial cadherin (VE-cadherin) in close cooperation with platelet and endothelial adhesion molecule-1 (PECAM-1) and nectin. VE-cadherin-mediated cell adhesion depends on extracellular Ca^{2+}, but not those mediated by PECAM-1 and nectin. TJs are made up of junctional adhesion molecule (JAM) family members, occuludin, claudin-5, and nectin (reviewed in Dejana, 2004).

VE-cadherin has an extracellular domain constituted by five cadherin domains, a transmembrane domain, and a cytoplasmic domain connected to p120 catenin and β-catenin (Iyer *et al.*, 2004). Through β-catenin, VE-cadherin is linked to α-catenin that is associated with the actin cytoskeleton, which results in the maintenance of cell–cell adhesion in conjunction with cytoskeleton (Herren *et al.*, 1998; Navarro *et al.*, 1998; Kobielak and Fuchs, 2004). Tyrosine-phosphorylated VE-cadherin in its cytoplasmic domain provides docking sites for signal-transmitting molecules (Esser *et al.*, 1998; Zanetti *et al.*, 2002; Hudry-Clergeon *et al.*, 2005). Conversely, cytoplasmic domain modified by phosphorylation or associated with signaling molecules triggers the inside-out signal that regulates the VE-cadherin-mediated cell adhesion (Nwariaku *et al.*, 2004). β-catenin binds to other signaling molecules including PI3-K and MAGUK with inverted domain structure-1 (MAGI-1) as well as α-catenin (Kotelevets *et al.*, 2005).

MAGI-1 consists of six PSD95/DiscLarge/ZO-1 (PDZ) domains, a guanylate kinase domain and two WW domains flanked by the first and second PDZ domain (Dobrosotskaya *et al.*, 1997). Because PDZ domains are docking domains for PDZ-binding molecules, MAGI-1 associates with a variety molecules such as NMDA (*N*-methyl-D-aspartate) receptors, PTEN, BAI-1, δ-catenin, mNET1, and β-catenin (Hirao *et al.*, 1998; Ide *et al.*, 1999;Mino *et al.*, 2000; Dobrosotskaya, 2001). These MAGI-1-associating molecules function at cell–cell contacts (Laura *et al.*, 2002). MAGI-1, therefore, functions as a scaffold molecule by localizing to cell–cell contacts. Recently, MAGI-1 is reported to biochemically form a complex with E-cadherin and β-catenin (Kawajiri *et al.*, 2000). How-

This article was published online ahead of print in *MBC in Press* (http://www.molbiolcell.org/cgi/doi/10.1091/mbc.E05-07-0647) on December 7, 2005.

[D] [V] The online version of this article contains supplemental material at *MBC Online* (http://www.molbiolcell.org).

Address correspondence to: Naoki Mochizuki (nmochizu@ri.ncvc.go.jp).

Abbreviations used: AJ, adherens junction; CFP, cyan fluorescent protein; ECM, extracellular matrix; EGFP, enhanced green fluorescent protein; FRET, fluorescence resonance energy transfer; GEF, guanine nucleotide exchange factor; GAP, GTPase activating protein; HAEC, human aortic endothelial cell; HUVEC, human umbilical vascular endothelial cell; JAM, junctional adhesion molecule; MAGI-1, MAGUK with inverted domain structure-1; GFP, green fluorescent protein; PBS, phosphate-buffered saline; PDZ, PSD95/DiscLarge/ZO-1; PECAM-1, platelet and endothelial cell adhesion molecule-1; siRNAs, small interfering RNAs; TJ, tight junction; VE-cadherin, vascular endothelial cadherin; VEC-Fc, recombinant VE-cadherin ectodomain-Fc chimera; YFP, yellow fluorescent protein.

ever, the role of the E-cadherin/β-catenin–MAGI-1 complex in cell–cell junctional formation remains elusive.

Rap1 regulates cell–cell adhesion as well as cell–extracellular matrix (cell-ECM) adhesion (Bos, 2005). We have previously demonstrated that Epac-Rap1 signaling enhances VE-cadherin-dependent cell adhesion, thereby stabilizing vascular endothelial cell junctions (Fukuhara *et al.*, 2005). On cell–cell contact, C3G, a guanine nucleotide exchange factor (GEF) for Rap1, is involved in the signaling mediated by E-cadherin and nectin in epithelial cells (Hogan *et al.*, 2004; Fukuyama *et al.*, 2005). Rap1 cycles between GDP-bound inactive form and GTP-bound active form; Rap1-specific GEFs and GTPase activating proteins (GAPs) activate and inactivate Rap1, respectively. Rap1 GEF family consists of C3G (RAPGEF1), PDZ-GEF1 (RAPGEF2), PDZ-GEF2, CalDAG-GEF1, Epac, and Epac2 (Bos *et al.*, 2001).

We here investigate the involvement of MAGI-1–PDZ-GEF1 in the activation of Rap1 on vascular endothelial cell contact and demonstrate that MAGI-1 recruited to cell–cell junctions by associating β-catenin contributes to cell–cell contact-dependent activation of Rap1. In addition, the MAGI-1-mediated signal evoked upon cell–cell contact augments VE-cadherin-dependent endothelial cell adhesion. Thus, engagement of VE-cadherin activates Rap1 via MAGI-1, resulting in positive regulation of VE-cadherin-mediated cell adhesion.

MATERIALS AND METHODS

Plasmids and Adenovirus

pRaichu-Rap1, Rap1 activation monitoring-probe based on fluorescence resonance energy transfer (FRET), and Adeno-Raichu-Rap1, an adenovirus expressing Raichu-Rap1 were described previously (Mochizuki *et al.*, 2001). Adenoviruses encoding Rap1GAPII and LacZ were obtained from S. Hattori (The Institute of Medical Science, University of Tokyo) and M. Matsuda (Research Institute for Microbial Disease, Osaka University, Osaka, Japan), respectively. Endothelial cells were infected with adenovirus at the appropriate multiplicity of infection for more than 24 h before imaging. The coding sequences of human MAGI-1b (hereafter MAGI-1) and PDZ-GEF1 were amplified by PCR using human heart cDNA library as a template and resultant DNAs were inserted into p3× FLAG-CMV-10 (Sigma, St. Louis, MO) and pEGFP-C1 (Clontech, Palo Alto, CA). cDNAs encoding truncated MAGI-1 as indicated in Figures 3B and 4A were similarly inserted into pEGFP-C1. pCALwL-FLAG-C3G, a FLAG-tagged mammalian expression vector, was obtained from M. Matsuda (Research Institute for Microbial Disease, Osaka University, Osaka, Japan; Ohba *et al.*, 2001). pJRM21-PDZ5 expressed FLAG-tagged PDZ domain 5 of MAGI-1 and internal ribosomal entry site-driven dsFP593 (Nagashima *et al.*, 2002). HcRed-p120 catenin-expressed HcRed-tagged p120 catenin was described previously (Kogata *et al.*, 2003).

Reagents and Antibodies

Purified human immunoglobulin (Ig) G Fc protein was purchased from ICN Biologicals (Cosa Mesa, CA). Glutathione Sepharose, protein A- and G-Sepharose were purchased from Amersham Biosciences (Piscataway, NJ). The rabbit polyclonal anti-MAGI-1b and anti-PDZ-GEF1 antibodies were developed in our laboratory by immunizing rabbits with recombinant glutathione S-transferase (GST)-tagged MAGI-1b (aa 1–140) or PDZ-GEF1 (aa 1–250) coupled with complete Freund's adjuvant, respectively. Anti-green fluorescent protein (GFP) antibody was generated in our laboratory. Other antibodies were purchased as follows: anti-Rap1 from Santa Cruz Biotechnology (Santa Cruz, CA); anti-FLAG (M2) and anti-vinculin from Sigma; anti-VE-cadherin, and anti-β-catenin from BD Bioscience (San Jose, CA); anti-ZO-1 from Zymed (South San Francisco, CA), Alexa 488- or Alexa 546-labeled secondary antibodies from Molecular Probes (Eugene, OR); horseradish peroxidase-coupled goat anti-mouse and anti-rabbit IgG from Amersham Biosciences.

Cell Culture and Transfection

Human umbilical vein endothelial cells (HUVECs) and human arterial endothelial cells (HAECs) were purchased from Kurabo (Kurashiki, Japan). The cells were maintained in HuMedia-EG2 with a growth additive set as described previously (Nagashima *et al.*, 2002). Bovine aortic endothelial cells (BAECs), MDCK and 293T cells were maintained in DMEM (Nissui, Tokyo, Japan) supplemented with 10% fetal bovine serum and antibiotics (100 μg of streptomycin and 100 U of penicillin/ml). Endothelial cells and 293T cells were transfected by LipofectAMINE plus reagent (Invitrogen, Carlsbad, CA) and by the calcium phosphate method, respectively.

FRET Imaging and Fluorescence Imaging

HUVECs cultured on collagen-coated glass-base dishes were infected with Adeno-Raichu-Rap1 or transfected with pRaichu-Rap1. The structure of Raichu-Rap1 and the principle of FRET are illustrated as in Figure 1A. Cells were imaged on an Olympus IX-81 inverted fluorescence microscope (Lake Success, NY) as described previously (Nagashima *et al.*, 2002). Dual images for cyan fluorescent protein (CFP) and yellow fluorescent protein (YFP) were obtained through an XF1071 excitation filter, an XF2034 dichroic filter, and an XF3075 emission filter for CFP and an XF 3079 for YFP (Omega Scientific, Tarzana, CA), respectively. The ratio image of YFP/CFP were created by MetaMorph 5.0 software (Universal Imaging, West Chester, PA) and displayed as an intensity-modulated display image as described previously (Nagashima *et al.*, 2002).

Quantitative FRET analysis at the cell–cell contacts was performed by dividing the intensity of YFP by that of CFP in the area defined by randomly selected 30 cell–cell contact sites. The detail was explained in the figure legend of Supplementary Figure 2. Cells expressing either fluorescence-tagged proteins (GFP, dsFP593, and HcRed) were time-lapse imaged similar to FRET imaging on an IX-81 microscope using appropriate filter sets for GFP and dsFP593.

Calcium Switch

HUVECs serum-starved for 10 h in medium 199 (Invitrogen) containing 1% bovine serum albumin (BSA) were transiently exposed to 4 mM EGTA for 30 min to chelate extracellular calcium and disrupt Ca^{2+}-dependent intercellular junctions (Volberg *et al.*, 1986). After washing, the cells were allowed to recover in complete cell calcium-containing culture media for the time indicated in the figure.

Detection of GTP-bound Rap1

GTP-bound active Rap1 was detected according to Bos's method (Franke *et al.*, 1997). Briefly, cells starved in medium 199 containing 1% BSA for 10 h were subjected to a calcium switch or stimulated with 10 μg/ml VE-cadherin ectodomain-Fc (VEC-Fc) protein for the time indicated at the top of the figure. The cells were lysed at 4°C in pulldown lysis buffer (20 mM Tris-HCl [pH 7.5], 100 mM NaCl, 10 mM $MgCl_2$, 1% Triton X-100, 1 mM EGTA, 1 mM dithiothreitol, 1 mM Na_3VO_4, 1× protease inhibitor cocktail). Precleared lysates were incubated with GST-Rap1 binding domain of RalGDS precoupled to glutathione-Sepharose beads. Proteins collected on the beads were subjected to SDS-PAGE followed by immunoblotting with anti-Rap1 antibody.

Immunocytochemistry and Confocal Imaging

Cells cultured on glass-bottom dishes were fixed with 2% formaldehyde in phosphate-buffered saline (PBS) for 30 min and permeabilized with 0.1% Triton X-100 for 10 min. Cells were blocked with 3% BSA for 30 min and incubated with anti-MAGI-1b, anti-VE-cadherin, anti-ZO-1, anti-vinculin, or anti-β-catenin antibody for 1 h at room temperature. Immunopositive reaction was visualized with Alexa 488- or Alexa 546-labeled secondary antibodies. Confocal images were obtained by an Olympus BX50WI microscope controlled by Fluoview.

Immunoprecipitation Assay

HUVECs were lysed with lysis buffer (100 mM NaCl, 50 mM Tris-HCl [pH 7.5], 1% Triton X-100, 2 mM Na_3VO_4, 1× protease inhibitor cocktail). Precleared cell lysates by centrifugation at 15,000 × *g* were incubated with antibodies. Immunoprecipitates collected on protein A- or G-Sepharose were subjected to SDS-PAGE and immunoblotting with antibodies as indicated in the figure.

siRNA-mediated Protein Knockdown

Small interfering RNAs (siRNAs) targeted to human MAGI-1; 5′-GGACCCUUCUCAGAAGUUCCCUCAA-3′ and 5′-UUGAGGGAACUUCUGAGAAGGGUCC-3, corresponding to nt 843–867 of coding sequence of MAGI-1 cDNA, and that for PDZ-GEF1; 5′-GGGAGUAAUCAAACAAAGAAGACUU3′ and 5′-AAGUCUUCUUUGUUUGAUUACUCCC3′, corresponding to nt 1980–2004 of PDZ-GEF1, were obtained from Invitrogen. VE-cadherin siRNAs were purchased from Santa Cruz Biotechnology. As a control, siRNA duplex with an irrelevant sequence was used. HUVECs were transfected with 20 nM siRNA duplexes using LipofectAMINE 2000 (Invitrogen) according to the manufacturer's instructions and incubated for 48 h after replacing fresh HuMedia-EG2.

Cell Adhesion Assay

Recombinant VEC-Fc chimeric protein was prepared as described previously (Fukuhara *et al.*, 2005). Twenty-four-well tissue culture plates were coated

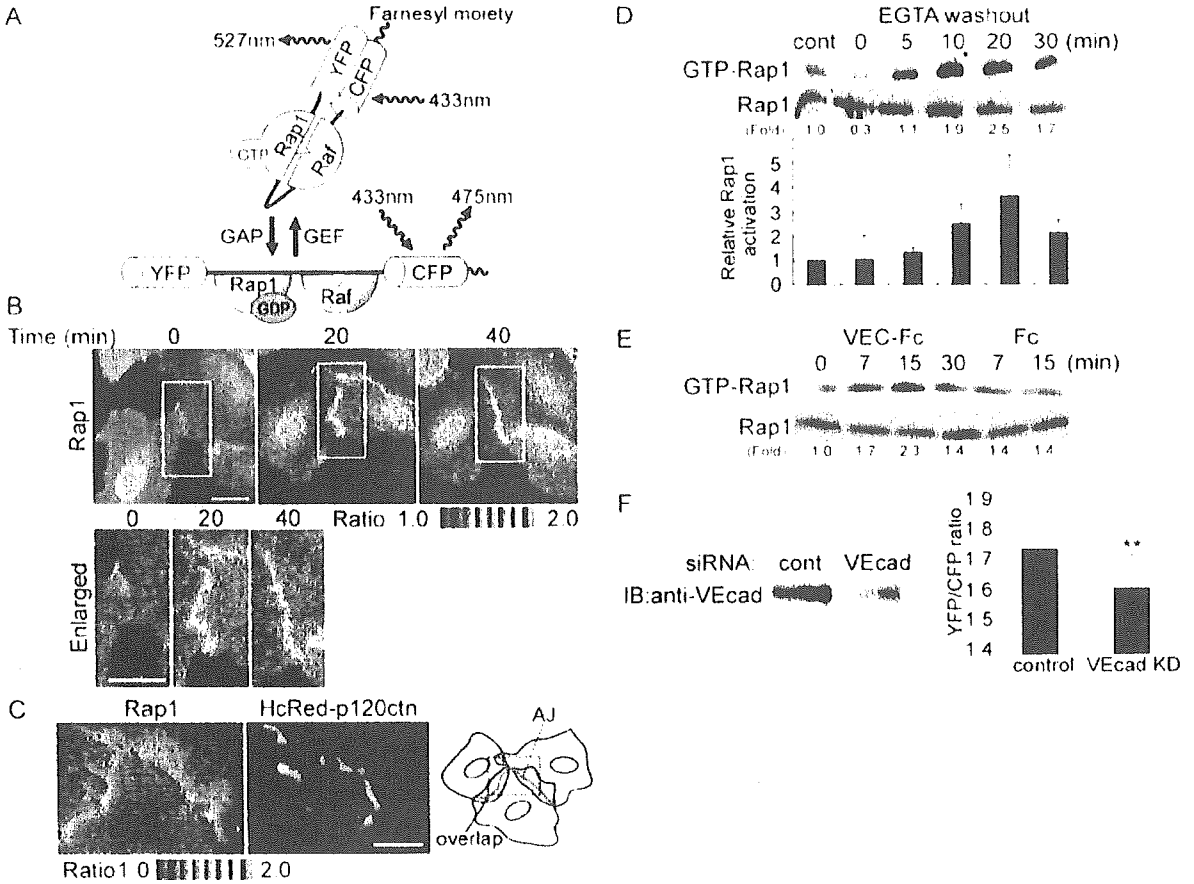

Figure 1. Rap1 is activated by VE-cadherin-mediated cell adhesion upon cell–cell contact. (A) Schematic illustration of Raichu-Rap1. FRET efficiency depends on the guanine nucleotide binding state of Rap1. GDP-bound Raichu-Rap1 emits 475-nm fluorescence when excited at 433 nm, whereas GTP-bound Raichu-Rap1 emits 527-nm fluorescence due to FRET. *Raf*; Ras/Rap1 binding domain of Raf. (B) Motile HUVECs infected with Adeno-Raichu-Rap1 were monitored by FRET time-lapse imaging every 20 s. A ratio image of YFP to CFP reflects FRET efficiency. Ratio images are shown by the intensity modulated display, in which the upper and lower limits of the ratio (the intensity of YFP divided by that of CFP) are indicated by the red and blue hues, respectively, and the average intensity of YFP and CFP is used. Time since starting FRET imaging is indicated on the top (min). The boxed regions in the top panels were enlarged and are shown in the bottom panels. Bars, 20 μm. (C) HUVECs expressing both Raichu-Rap1 and HcRed-tagged p120 catenin were FRET-imaged and red-fluorescence-imaged. The real images of boxed region of the schema are shown as FRET image (left panel) and red-fluorescence image (center). Areas indicated by the gray are regions where protruding and overlapping regions of the contacting cells. Note that Rap1 is activated at the adherens junctions where p120 catenin localizes. Bar, 20 μm. (D) Confluent HUVECs cultured in medium 199 containing 1% BSA without serum were treated with EGTA for 30 min to disrupt Ca^{++}-dependent cell adhesion. Subsequently, the cells were treated with Ca^{++}-containing medium. Cell lysates at the time points indicated at the top were subjected to pulldown assay for detecting GTP-bound Rap1 as described in *Materials and Methods*. A representative results from three independent experiments is shown (top). Fold activation indicates the ratio of the GTP-Rap1 intensity of total Rap1 intensity to the control GTP-Rap1 intensity of total Rap1 intensity. The result from three independent experiments were shown (bottom). Control (cont) was prepared from cells in medium 199 before calcium switch. Cells treated with EGTA for 30 min (time 0). (E) HUVECs sparsely cultured on the dish were stimulated with 10 μg/ml VEC-Fc or Fc for the time indicated at the top. Rap1 activity was examined as described for D. Fold activation is analyzed similarly to D. (F) The effect of VE-cadherin siRNA on VE-cadherin expression was examined by immunoblotting (left). FRET at the cell–cell contacts were quantitatively analyzed in control siRNA treated HUVECs and VE-cadherin-depleted HUVECs (right), as explained in Supplementary Figure 2. Mean values with SDs obtained by 30 cell–cell contact sites are shown as a representative result of three independent experiments. Statistical significance was analyzed by Student's *t* test: ** $p < 0.01$.

with 10 μg VEC-Fc or Fc protein/ml in PBS Ca^{++}/Mg^{++} overnight at 4°C followed by blocking with 1% heat inactivated BSA in PBS (inactivated at 85°C for 12 min) for 1 h at room temperature. HUVECs treated with control siRNAs or MAGI-1 siRNAs were cultured for 48 h and then suspended in 0.5% BSA-containing Medium 199. Resuspended cells, 2.0×10^5, were plated and adhered onto each VEC-Fc or Fc coated well at 37°C for the indicated time. To analyze cell adhesion to a collagen-covered surface, a collagen coated 24 well plate (Iwaki, Japan) was used instead of the VEC-Fc coated plate. After washing with PBS Ca^{++}/Mg^{++} four times to remove nonadherent cells, adherent cells and input cells were quantified by measuring endogenous alkaline phosphatase (AP) activity by using AttoPhos AP fluorescent substrate system (Promega, Madison, WI).

RESULTS

Rap1 Is Activated on Homophilic VE-Cadherin Association at Cell–Cell Contacts

Rap1 is previously reported to localize to cell–cell contacts in vascular endothelial cells as well as epithelial cells to stabilize cell–cell contacts (Mandell *et al.*, 2005; Wittchen *et al.*, 2005). However, it remains elusive where Rap1 is activated on cell contacts. To monitor the spatiotemporal activation of Rap1 on vascular endothelial cell–cell contact,

HUVECs expressing Raichu-Rap1 were time-lapse FRET-imaged. Raichu-Rap1 consists of YFP, Rap1, the Ras-binding domain of Raf, CFP, and a CAAX box of Ki-Ras. The intramolecular binding of GTP-Rap1 to Raf induces FRET from CFP to YFP (Figure 1A), whereas the dissociation of Rap1 from Raf reduces FRET. Increased FRET indicated by a red hue was observed at cell–cell contacts during spontaneous movement (Figure 1B and Supplementary Movie 1). Rap1 was constantly activated in the perinuclear region of the cells irrespective of cell–cell contact.

In vascular endothelial cells, the peripheral membrane of cells contacting each other was overlapped. Thus, AJs and TJs are intermingled (Dejana, 2004). To ascertain Rap1 activation at the adherens junctions, HUVECs expressing both Raichu-Rap1 and HcRed-tagged p120 catenin were imaged (Figure 1C). Most of Rap1 activation as indicated by red hue was observed at AJs where p120 catenin was localized. No remarkable Rap1 activation was detected within the protruding membrane overlapping region.

We further quantitatively examined whether the Rap1 is activated during cell adhesion after de-adhesion by chelating extracellular calcium and restoring calcium (hereafter, calcium switch). GTP-bound Rap1 was rapidly increased within 5 min and to a greater extent than the predisruption level by restoration of Ca^{2+} (Figure 1D, top panel). The quantitative results obtained from three independent experiments were shown (Figure 1D, bottom panel). These results suggest that the cell–cell contact triggers the Rap1 activation in a manner dependent on extracellular Ca^{2+}. Although Rap1 is reported to be activated in a manner dependent on nectin, which is independent of extracellular Ca^{2+} (Fukuyama *et al.*, 2005), we assumed that Ca^{2+}-dependent cell–cell contact triggers Rap1 activation besides nectin-triggered Rap1 activation. We, therefore, examined the VE-cadherin engagement-dependent Rap1 activation. To mimic the VE-cadherin engagement in nascent cell–cell contacts, we used VEC-Fc chimeric protein, which consisted of the extracellular domain of VE-cadherin fused to the Fc portion of Ig. GTP-bound Rap1 was increased when cells were treated with VEC-Fc, but not with control Fc (Figure 1E).

To examine the requirement of VE-cadherin for Rap1 activation upon cell–cell contact, we imaged Rap1 activation in VE-cadherin-depleted HUVECs. Quantitative FRET imaging analysis upon cell–cell contacts demonstrated that Rap1 activation at the cell–cell contacts was less in VE-cadherin-depleted cells than those observed in control siRNA-treated cells (Figure 1F). Collectively, these data indicate that the engagement of VE-cadherin induces Rap1 activation.

MAGI-1 Localizes to Cell–Cell Contacts and Binds to β-Catenin

MAGI-1 constitutes a complex with E-cadherin/β-catenin and associates with a GEF for Rap1, PDZ-GEF1 (Kawajiri *et al.*, 2000), implying that MAGI-1 may link the cadherin-mediated signal to PDZ-GEF1 for the activation of Rap1. To investigate the involvement of MAGI-1 in Rap1 activation on VE-cadherin-mediated cell–cell contact, we first developed an anti-MAGI-1 antibody and examined the expression of MAGI-1 in vascular endothelial cells. MAGI-1 was expressed in all cultured vascular endothelial cells we tested, because it was found in MDCK epithelial cells used as a positive control (Figure 2A). Next, we examined the localization of MAGI-1 in vascular endothelial cells by immunostaining. MAGI-1 was localized to the cell–cell contacts (Figure 2B) and colocalized with VE-cadherin (Figure 2C). The immunopositive reaction in the nucleus appeared to be non-

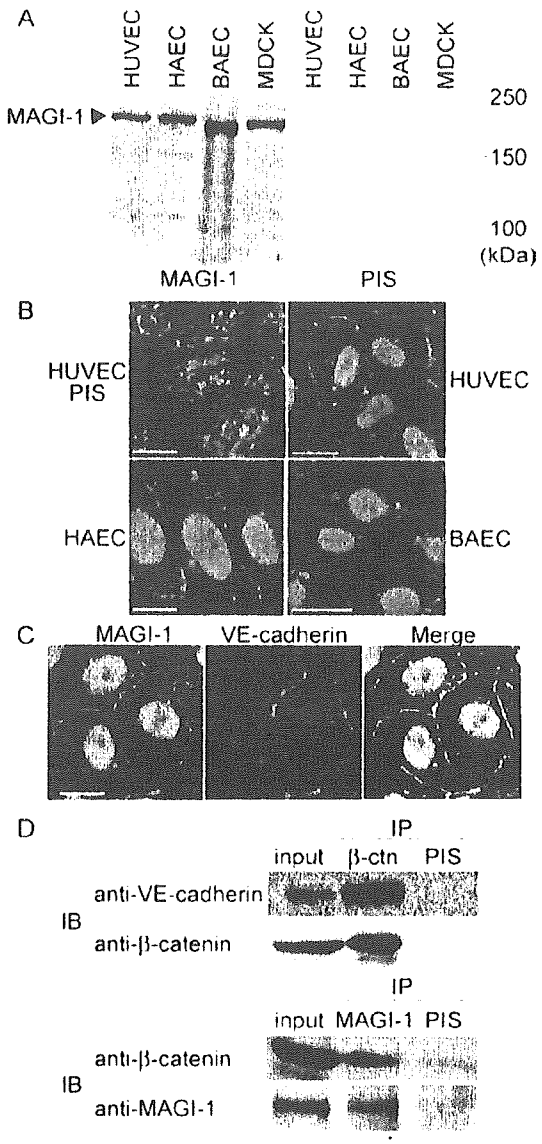

Figure 2. MAGI-1 localizes to cell–cell contacts and forms a complex with VE-cadherin and β-catenin. (A) Lysates from the cells indicated at the top were subjected to SDS-PAGE followed by immunoblotting with anti-MAGI-1 antibody (left) and with pre-immune serum (PIS, right). (B) Endothelial cells were immunostained with pre-immune serum (PIS, left top) and anti-MAGI-1 antibody. Immunoreaction was visualized by fluorescent microscopy. Bars, 20 μm. (C) HUVECs were immunostained with both anti-MAGI-1 antibody (green) and anti-VE-cadherin antibody (red). A merged image is shown in the right panel (Merge). Bar, 20 μm. (D) Cell lysates from HUVECs were subjected to either immunoprecipitation (IP) with antibodies as indicated at the top followed by immunoblotting (IB) with antibodies as indicated at the left. VE-cadherin was coimmunoprecipitated with β-catenin (top). β-catenin was coimmunoprecipitated with MAGI-1 (bottom)

specific, because it was detected in the nucleus by immunostaining using preabsorbed anti-MAGI-1 (unpublished data) and after knockdown of MAGI-1 (see Figure 5B).

To investigate how MAGI-1 localizes to cell–cell contacts, we tested the link between VE-cadherin and MAGI-1 by β-catenin. We examined this link by immunoprecipitation

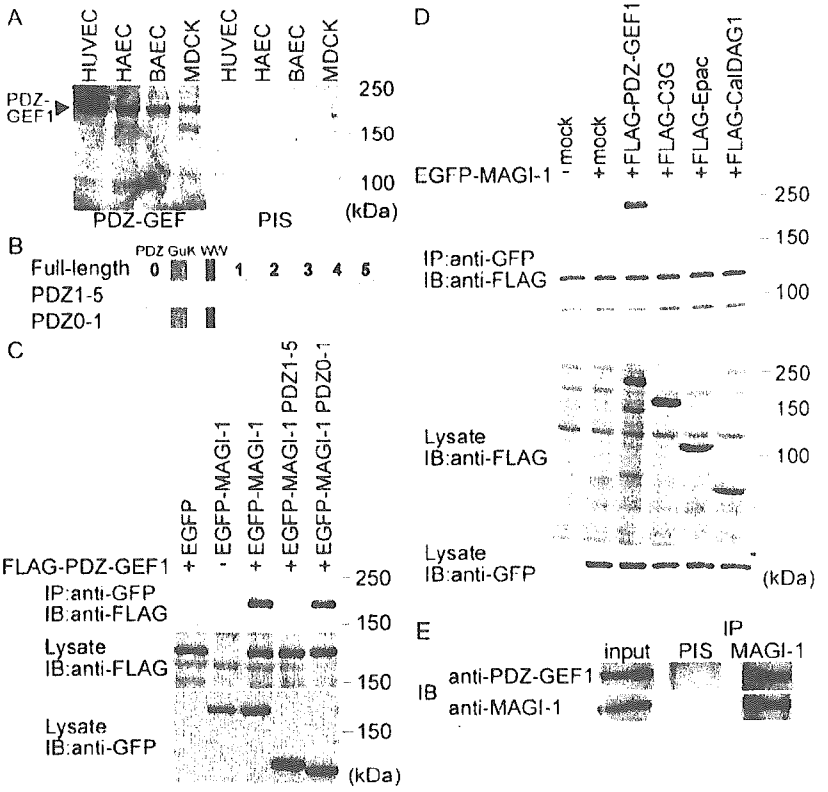

Figure 3. MAGI-1 interacts with PDZ-GEF1 in vascular endothelial cells. (A) Cell lysates from HUVECs, HAECs, BAECs, and MDCK cells were subjected to SDS-PAGE and immunoblotting with anti-PDZ-GEF1 antibody (left) or pre-immune serum (PIS, right). (B) Schematic illustration of MAGI-1 (full length) and its deletion mutants. MAGI-1 consists of six PDZ domains (PDZ0–5, indicated by gray boxes), a guanylate kinase domain (GuK), and two WW domains. Deletion mutants, PDZ1–5 and PDZ0–1, consist of PDZ1 to PDZ5 and the amino-terminus to PDZ1, respectively. (C) 293T cells were transfected with the plasmids together with (+) or without (−) FLAG-tagged PDZ-GEF1 expressing vector as indicated at the top. Cell lysates were subjected to immunoprecipitation (IP) with anti-GFP antibody followed by immunoblotting (IB) or directly to immunoblotting using the antibodies as indicated. Note that FLAG-tagged PDZ-GEF1 is coimmunoprecipitated with GFP-tagged PDZ0–1. (D) Cells transfected with a panel of FALG-tagged Rap1 GEF-expressing plasmids together with (+) or without (−) EGFP-tagged MAGI-1-expressing plasmid. Cell lysates were subjected to immunoprecipitation (IP) followed by immunoblotting (IB) similarly to C. Note that only FLAG-tagged PDZ-GEF-1 among several Rap1 GEFs is coimmunoprecipitated with MAGI-1. (E) The lysate of HUVECs was incubated with either pre-immune serum (PIS) or anti-MAGI-1 antibody, followed by immunoblotting with anti-PDZ-GEF1 antibody. Note that MAGI-1 is co-immunoprecipitated with PDZ-GEF1.

assay (Figure 2D). β-catenin bound to both VE-cadherin (Figure 2D, top panel) and MAGI-1 (Figure 2D, bottom panel). These results indicate that MAGI-1 appears to localize to VE-cadherin-based cell adhesion through β-catenin in vascular endothelial cells.

MAGI-1 Interacts with PDZ-GEF1 in Vascular Endothelial Cells

It has been shown that MAGI-1 binds to PDZ-GEF1 localized to cell–cell contacts in epithelial cells (Dobrosotskaya and James, 2000; Kawajiri *et al.*, 2000). We hypothesized that PDZ-GEF1 is associated with MAGI-1 in vascular endothelial cells and that it is involved in the activation of Rap1 on VE-cadherin-mediated cell–cell contact. PDZ-GEF1 was expressed in vascular endothelial cells similarly to MAGI-1 (Figure 3A). The interaction between MAGI-1 and PDZ-GEF1 was examined by the immunoprecipitation using the full-length and the truncated mutants of MAGI-1 (Figure 3, B and C). The PDZ-GEF1 bound to the N-terminus of MAGI-1 (Figure 3C). EGFP-tagged MAGI-1 coimmunoprecipitated PDZ-GEF1, but not other GEFs for Rap1, C3G, Epac1, and CalDAG-GEF-I (Figure 3D). We further examined the interaction between endogenous MAGI-1 and PDZ-GEF1 in HUVECs. Both MAGI-1 and PDZ-GEF1 were coimmunoprecipitated from the lysate of HUVECs (Figure 3E), indicating that PDZ-GEF1 associates with MAGI-1 in vascular endothelial cells.

Localization of MAGI-1 to Cell–Cell Contact is Important for Rap1 Activation on Cell Contact

To understand the role of MAGI-1 in activating Rap1 when forming cell–cell contacts, we proceeded to investigate the localization of MAGI-1 using EGFP-tagged MAGI-1 in motile endothelial cells. EGFP-MAGI-1 was accumulated at cell–cell contacts (Figure 4B, left panels, and Supplementary Movie 2). Removal of the carboxy terminal PDZ domain (delta PDZ5) resulted in the dissociation of MAGI-1 from cell–cell contacts (Figure 4B, right panels, and Supplementary Movie 3). Because it was reported that MAGI-1 binds to β-catenin through PDZ5 (Dobrosotskaya and James, 2000), we tested the requirement of PDZ5 for the association of MAGI1- with β-catenin. β-catenin was coimmunoprecipitated with EGFP-tagged full-length MAGI-1 but not with MAGI-1 lacking PDZ5 (Figure 4C). These results suggest that MAGI-1 localizes to vascular endothelial cell–cell contacts in a manner dependent on β-catenin. We further revealed that MAGI-1 was dislocated from the cell–cell contact of the PDZ5-expressing cells as marked by red fluorescence but not from that of wild-type cells (Figure 4D), indicating that PDZ5 is important for the localization of MAGI-1 to cell–cell contacts.

To examine the requirement of the association of MAGI-1 with β-catenin for the cell–cell contact-induced Rap1 activation, we checked the effect of disconnection of MAGI-1 to β-catenin by overexpressing MAGI-1 PDZ domain 5 on Rap1 activation. In HUVECs expressing MAGI-1 PDZ domain 5, as marked by dsFP593 (Figure 4E and Supplementary Movie 4), Rap1 activation upon cell–cell contacts was not observed in FRET imaging. These results indicate that the dislocation of MAGI-1 from the cell–cell contact inhibits Rap1 activation at the cell–cell contacts in motile vascular endothelial cells.

To confirm the requirement of MAGI-1 in Rap1 activation upon vascular endothelial cell–cell contact, we knocked down MAGI-1 in HUVECs using RNA interference. MAGI-1

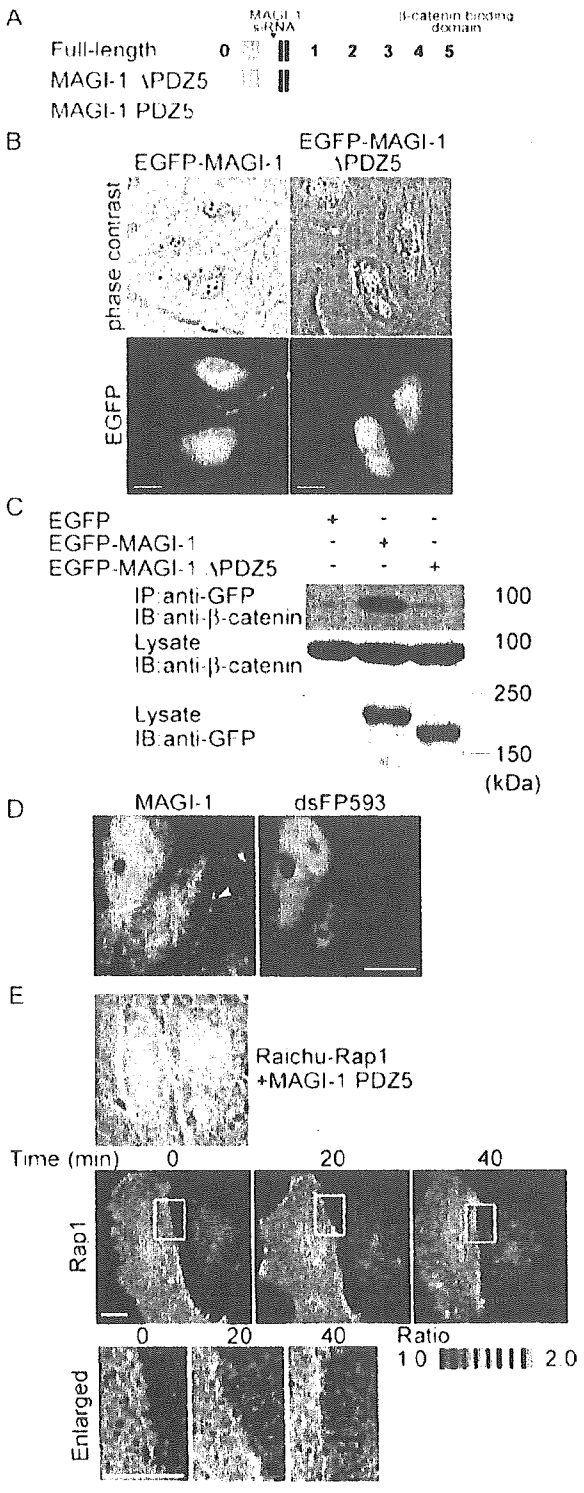

Figure 4. MAGI-1 localizing to cell–cell contact via β catenin is required for Rap1 activation. (A) Schematic illustration of MAGI-1 and its mutants. The corresponding region of siRNA for MAGI-1 used in Figure 5 is also indicated in this schema.(B) HUVECs were transfected with the plasmids indicated at the top and imaged on an Olympus IX-81 fluorescent microscope. Bars, 20 μm. Note the localization of EGFP-MAGI-1 at the cell–cell contact but not MAGI-1 lacking PDZ domain 5. (C) 293T cells were transfected with the plasmids as indicated at the top. Cell lysates were subjected to immunoprecipitation (IP) with anti-GFP followed by immunoblotting (IB) or directly to immunoblotting using the antibodies indicated at the left. Note that endogenous β-catenin is coimmunoprecipitated with EGFP-tagged MAGI-1, but not with that lacking PDZ5. (D) HUVECs expressing PDZ domain 5 of MAGI-1 was immunostained with anti-MAGI-1 antibody. No immunoreaction was detected at the cell–cell contact between PDZ domain 5-expressing cells (arrow), whereas immunoreaction was detected at the contact between PDZ domain 5-expressing cell and untransfected cell (arrowhead). (E) HUVECs transfected with Raichu-Rap1 and pIRM21-MAGI-1-PDZ5 were FRET-imaged (middle). Phase contrast image was overlaid onto the image for dsFP593 to distinguish HUVECs transfected with pIRM21-MAGI-1-PDZ5 from those transfected only with Raichu-Rap1 (top). Red and blue hues indicated by intensity modulated display reflect increased and decreased FRET, respectively. The boxed regions in the middle panels were enlarged (bottom). The upper and lower limits of the ratio range are shown at the bottom right. Bars, 20 μm.

was almost completely reduced, as examined by Western blotting (Figure 5A). MAGI-1 at the cell–cell junction was not found in the cells treated with siRNA, as examined by immunostaining (Figure 5B). In the same setting, siRNA-introduced HUVECs expressing Raichu-Rap1 were subjected to FRET imaging. Rap1 activation upon cell–cell contact was significantly suppressed in MAGI-1-depleted cells (Figure 5C and Supplementary Movie 5). Quantitative FRET imaging analysis was performed to quantitatively analyze the activation of Rap1 at the cell–cell contacts in MAGI-1-depleted cells (Figure 5D and Supplementary Figure 2). We notice that Rap1 activation was detected at the free ruffled membrane without cell–cell contacts, similarly to control cells (Supplementary Movies 1 and 5), even in the MAGI-1-depleted cells. Collectively, these data suggest that the localization of MAGI-1 to cell–cell contacts through binding to β-catenin is involved in Rap1 activation.

Depletion of MAGI-1 Results in Impairment of VE-Cadherin-based Cell Adhesion

To elucidate the role of activated Rap1 downstream of MAGI-1 upon cell–cell contact, we examined the effect of depletion of MAGI-1 on VE-cadherin/β-catenin-based cell–cell contact after calcium switch. The localization of VE-cadherin and β-catenin at cell–cell contacts in confluent monolayer-cultured HUVECs was unchanged by MAGI-1 siRNA treatment. Because calcium switch induces cadherin-mediated cell junction after its disruption, we looked at the localization of VE-cadherin and β-catenin during calcium switch by immunostaining for VE-cadherin and β-catenin. VE-cadherin was reaccumulated at cell–cell junctions together with β-catenin within 20 min in control HUVECs. In clear contrast, there was a significant impairment of the formation of VE-cadherin/β-catenin-based cell junction in MAGI-1-depleted HUVECs (Figure 6).

TJ formation was not affected by MAGI-1 depletion and calcium switch (Figure 7A), whereas the recovery of VE-cadherin-based cell adhesion was substantially impaired in MAGI-1-depleted cells. These results indicate that MAGI-1-mediated signal is important for VE-cadherin/β-catenin-based cell adhesion.

We and others have previously reported that Rap1 activation enhances cell adhesions (Fukuhara *et al.*, 2005; Kooistra *et al.*, 2005). Cortical actin formation is enhanced by Rap1 activation and strengthens VE-cadherin-based cell–cell adhesion. Vinculin supports the cortical actin by linking α-catenin to α-actinin and by directly functioning as an

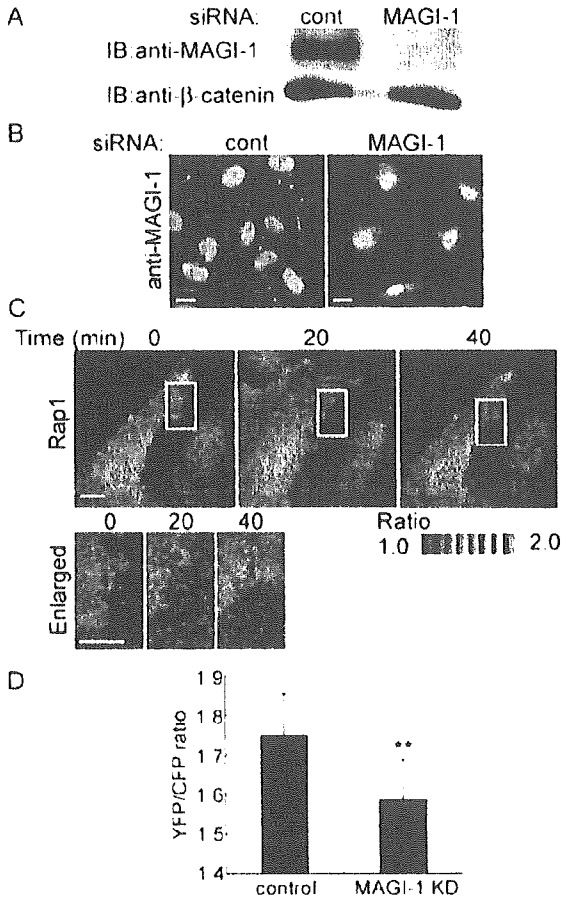

Figure 5. Depletion of MAGI-1 inhibits Rap1 activation upon cell–cell contact. (A) HUVECs transfected with control siRNAs or MAGI-1 siRNAs were cultured for 48 h. The cells were lysed, subjected to SDS-PAGE, and immunoblotted with anti-MAGI-1 and anti-β-catenin. (B) HUVECs transfected with control siRNAs or MAGI-1 siRNAs were cultured for 48 h and immunostained with anti-MAGI-1. Bars, 20 μm. (C) MAGI-1-depleted HUVECs were infected with Adeno-Raichu-Rap1 and FRET-imaged. The ratio-images indicate Rap1 activation by red hue and Rap1 inactivation by blue hue (top). The boxed region between two neighboring cells is enlarged (bottom). Bars, 20 μm. (D) Quantitative FRET analysis at the cell–cell contacts were performed in cells treated with control siRNA-treated HUVECs (control) and with MAGI-1-depleted cells (MAGI-1 KD). Quantitative FRET analysis is explained in Supplementary Figure 2. Mean values with standard deviations obtained by 30 cell–cell contact sites are shown as a representative result of three independent experiments. Statistical significance was analyzed by Student's *t* test and is indicated as ** $p < 0.01$.

actin-bundling molecule (Kobielak and Fuchs, 2004). Thus we investigated the vinculin localization after calcium switch by immunostaining. Vinculin was observed at the cell-ECM contacts presumably by translocating from cell–cell contacts after calcium depletion. Calcium restoration induced the relocation of vinculin from cell-ECM to cell–cell contact in control siRNA-treated cells. In clear contrast, vinculin remained at the focal adhesions in MAGI-1-depleted cells after calcium switch (Figure 7B). These data suggest that MAGI-1-dependent Rap1 activation at cell–cell contact may affect the vinculin localization, thereby regulating VE-cadherin-based cell adhesion.

MAGI-1 Is Required for VE-Cadherin-mediated Cell Adhesion

Vascular endothelial cell adhesion entails VE-cadherin-based adhesion and other cell adhesion molecules-based cell adhesion. To directly assess the involvement of MAGI-1 in VE-cadherin-mediated cell adhesion, we examined the adhesion of control siRNA-treated HUVECs and MAGI-1-depleted HUVECs onto VEC-Fc-coated dishes. The adhesion was quantified by the ALP activity of cells attaching to the dish after washing. Control HUVECs adhered to the VEC-Fc-coated dish in a time-dependent manner, whereas MAGI-1-depleted HUVECs exhibited significantly impaired adhesion to the VEC-Fc-coated dish (Figure 7A). No cells attached to the Fc-coated dish. MAGI-1-depleted HUVECs adhered to the collagen-coated dish comparably to control HUVECs (Figure 7B). We proceeded to examine the effect of inactivation of Rap1 on VE-cadherin-dependent adhesion. Control adenovirus-infected HUVECs adhered to VEC-Fc-coated dish, whereas Rap1GAPII-expressing adenovirus-infected HUVECs did not (Figure 7C). These results indicate that MAGI-1 and Rap1 activation is required for VE-cadherin-dependent cell adhesion.

DISCUSSION

FRET imaging enabled us for the first time to show the activation of Rap1 at the endothelial cell–cell junction, although previously Rap1 was suggested to be activated upon cell adhesion. In epithelial cells, C3G associating with E-cadherin is responsible for Rap1 activation upon cell contacts (Hogan *et al.*, 2004). Rap1, vice versa, regulates E-cadherin-mediated cell adhesion (Price *et al.*, 2004). In addition to E-cadherin, homophilic dimerization of nectin at the AJs triggers Rap1 activation downstream of Src-Crk (Fukuyama *et al.*, 2005). During the calcium switch experiment, which requires extracellular Ca^{2+}, we found that Rap1 was activated (Figure 1C), indicating extracellular Ca^{2+}-dependent signal, namely cadherin- and nectin-independent signal, appears to be involved in Rap1 activation upon cell–cell contact. In the present study, we propose the involvement of the MAGI-1/PDZ-GEF1 complex in Rap1 activation, besides nectin-mediated Rap1 activating signal and the subsequent positive feedback regulation of VE-cadherin-mediated cell adhesion.

Rap1 is responsible for maintenance and maturation of AJs. The establishment of cadherin-dependent cell–cell contacts is attributable to Rap1 in *Drosophila melanogaster* and mammalian cells (Knox and Brown, 2002; Price *et al.*, 2004). Consistently, we show here that VE-cadherin-dependent cell adhesion triggers a signal implicating MAGI-1 in Rap1 activation, presumably the MAGI-1–PDZ-GEF1-Rap1 pathway. VE-cadherin engagement-induced Rap1 activation may contribute to AJ formation in addition to homophilic engagement of nectin-dependent Rap1 activation (Fukuyama *et al.*, 2005).

Here we demonstrate VE-cadherin-dependent Rap1 activation besides nectin-dependent Rap1 activation. Calcium switch does not alter localization of nectin at the cell–cell contacts (Yamada *et al.*, 2005). We found that Rap1 was activated after calcium restoration in the calcium switch experiment that mimics nascent cell–cell contact formation (Figure 1), indicating that Ca^{2+}-dependent cell–cell contact is involved in Rap1 activation. We first assumed that VE-cadherin is responsible for Rap1 activation. Indeed, VE-cadherin depletion inhibited cell–cell contact-mediated Rap1 activation (Figure 1F).

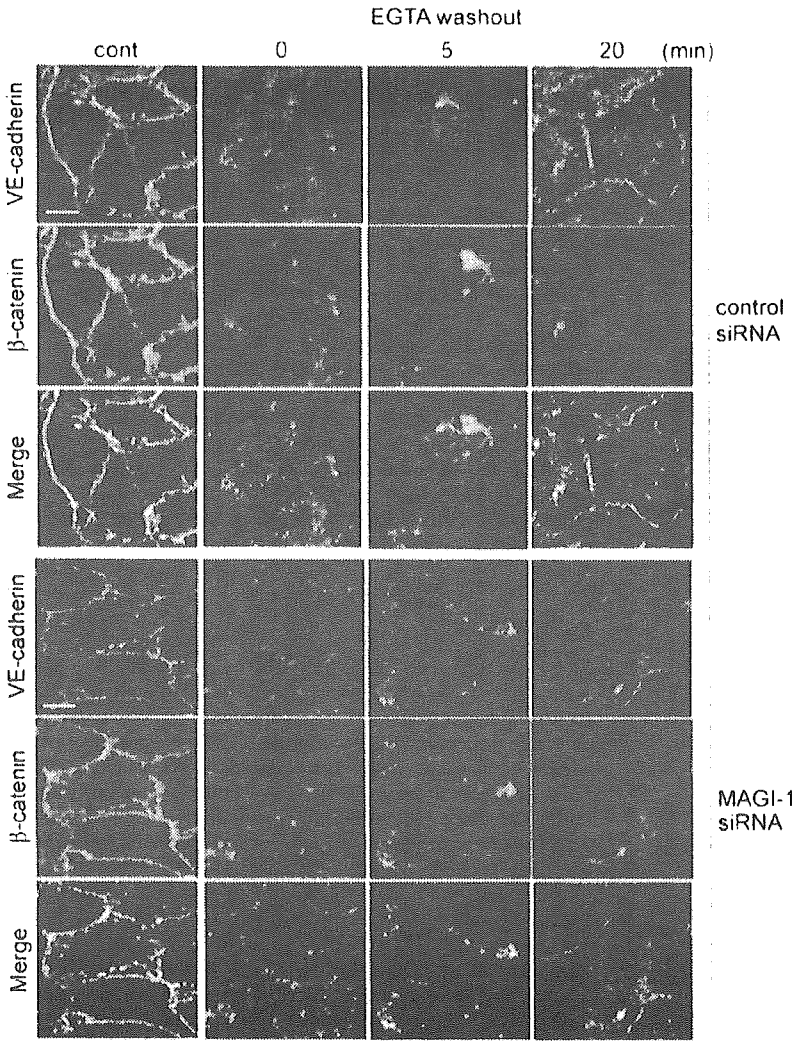

Figure 6. Depletion of MAGI-1 impairs AJ formation. HUVECs transfected with control siRNAs (top three columns) or MAGI-1 siRNAs (bottom three columns) were cultured for 48 h. Cells were replated onto the glass-base dishes for another 24 h to constitute the cell–cell contacts. The cells were treated with EGTA for 30 min to disrupt VE-cadherin-dependent junctions and kept in the replaced medium containing Ca^{++} for the time indicated at the top. The cells were immunostained with anti-VE-cadherin antibody (green) and anti-β-catenin antibody (red). The merged images are shown in the bottom panels (Merge). Bars, 20 μm. VE-cadherin remarkably accumulated 20 min after Ca^{++} restoration in control siRNA-treated HUVECs, whereas slight accumulation was observed in MAGI-1 siRNA-treated HUVECs.

These two AJ molecules, VE-cadherin and nectin, are linked by their cytoplasmic domain-associating proteins (Tachibana *et al.*, 2000). L-afadin, a nectin cytoplasmic domain-binding molecule, binds to α-catenin and subsequently locates cadherin to AJs without the transinteraction of cadherin (Tanaka *et al.*, 2003). L-afadin, s-afadin (AF-6), and Canoe (*Drosophila* orthologue of AF-6) contain a Rap1-binding domain (Boettner *et al.*, 2000, 2003). Thus, afadin regulated by activated Rap1 at cell–cell contacts may enhance AJ formation constituted by both cadherin and nectin.

We explored the requirement of MAGI-1 for Rap1 activation at cell adhesion. The association of MAGI-1 with β-catenin via the PDZ domain 5 is critical for its localization to VE-cadherin-based cell–cell contact. MAGI-1 also interacts with endothelial cell-selective adhesion molecule (ESAM) and JAM-4 at TJs (Hirabayashi *et al.*, 2003). Other JAM family members (JAM-A, B, and C) do not bind to MAGI-1 (our unpublished data). The carboxy-terminal sequence of ESAM and JAM-4 provides the class I PDZ-binding motif, whereas that of JAM family members contains the class II PDZ-binding motif (Hung and Sheng, 2002). Thus, ESAM-mediated MAGI-1 recruitment may contribute to Rap1-regulated cell adhesion at TJs as β-catenin recruits MAGI-1 at AJs. It will be interesting to explore the TJ-dependent Rap1 activation.

MAGI-1 together with MAGI-2 (S-SCAM), and MAGI-3 constitute the MAGI family (Hirao *et al.*, 2000; Franklin *et al.*, 2005). It has been shown that MAGI-2 binds to β-catenin and that MAGI-3 colocalized to β-catenin in astrocytes expressing E-cadherin (Adamsky *et al.*, 2003; Subauste *et al.*, 2005). Although MAGI-2 is exclusively expressed in the brain, MAGI-3 is ubiquitously expressed. Although we cannot exclude the involvement of MAGI-3 in the activation of Rap1 in vascular endothelial cells, the disconnection of MAGI family members from β-catenin by overexpressing the PDZ domain 5 of MAGI-1 perturbed the Rap1 activation upon cell–cell contact (Figure 4, D and E). Furthermore, depletion of MAGI-1 by siRNA hampered the Rap1 activation (Figure 5), suggesting that MAGI-1 is indispensable for Rap1 activation based on the linkage between VE-cadherin-β-catenin complex and MAGI-PDZ-GEF1 complex in vascular endothelial cells.

To delineate the VE-cadherin engagement-triggered Rap1 activation signal, we tried to test the requirement of

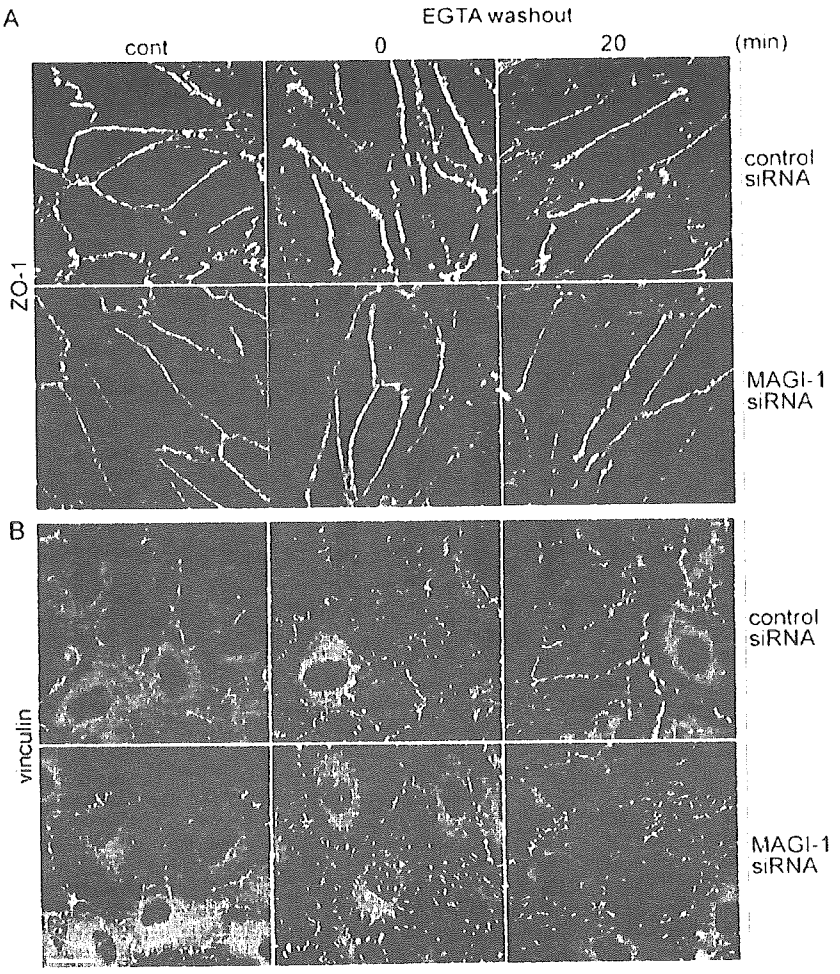

Figure 7. MAGI-1 depletion affects an AJ-supporting molecule, vinculin, but not a TJ-supporting molecule, ZO-1. (A) Similarly to Figure 6, HUVECs treated with control siRNAs (top panels) and MAGI-1 siRNAs (bottom panels) were immunostained with anti-ZO-1 after calcium switch. Bar, 20 μm. Note that ZO-1-positive cells were affected neither by calcium switch nor MAGI-1 depletion. (B) Similarly to A, control siRNA-treated cells and MAGI-1-depleted cells were immunostained with anti-vinculin before and after Ca^{2+} switch. Ca^{2+} depletion from the culture medium resulted in displacement of vinculin from cell–cell contacts to cell-ECM contacts and Ca^{2+}-restoration induced relocalization from cell-ECM contacts to cell–cell contacts in control HUVECs. In clear contrast, vinculin remained at the cell-ECM contacts even 20 min after Ca^{2+} restoration in MAGI-1-depleted cells.

PDZ-GEF1 for Rap1 activation because we found that MAGI-1 associated with PDZ-GEF1 in vascular endothelial cells (Figure 3), as this association reported previously (Dobrosotskaya and James, 2000; Kawajiri *et al.*, 2000). PDZ-GEF1-depleted cells seemed to be detached from the collagen-coated dishes and the adhesive activity to collagen-coated dish was significantly inhibited. Thus we assumed that there might be other signaling besides MAGI-1–PDZ-GEF1-mediated signal for cell adhesion and thus concluded that PDZ-GEF1-depleted cells were not appropriate for further evaluation to delineate the signaling. At least, VE-cadherin engagement-triggered Rap1 activation requires MAGI-1.

Activated Rap1 upon cell–cell contact further strengthens the VE-cadherin-dependent cell–cell adhesion. Rap1 activation is required for VE-cadherin-mediated cell adhesion (Figure 8B). We previously reported that the inside-out signal regulated by cAMP-Epac-Rap1 signal enhances the VE-cadherin-mediated cell–cell contacts by regulating cortical actin (Fukuhara *et al.*, 2005). Although we did not observe significant cortical actin distribution after calcium switch experiment (unpublished data), we noticed that the relocation of vinculin from cell-ECM to cell–cell contacts was inhibited in MAGI-1-depleted cells. Because vinculin supports the cadherin-based cell contacts by linking actin to cytoplasmic domain of cadherin through α-catenin, inhibition of Rap1 activation by MAGI-1 depletion might affect AJ formation. These results imply a positive feedback loop in cell–cell contact regulated by Rap1; namely, cell–cell contact promotes transdimerization of cell surface adhesion molecules, inducing Rap1 activation followed by further tightening of VE-cadherin-mediated cell adhesion.

In conclusion, we revealed that MAGI-1 is required for Rap1 activation upon cell–cell contacts and in turn for AJ formation. The translocation of MAGI-1 to cell–cell contacts is ascribed to its association with β-catenin. The MAGI-1-associating molecule, PDZ-GEF1, may account for Rap1 activation.

ACKNOWLEDGMENTS

We are grateful to M. Matsuda for his advice, plasmids, and virus; K. Kaibuchi for anti PDZ-GEF1 antibody; I. T. Pearson for his critical reading of this manuscript; and M. Sone, Y. Mizushima, and Y. Matsumura for their technical assistance. This work was supported by grants from the Ministry of Health, Labor, and Welfare Foundation of Japan; from the Program for Promotion of Fundamental Studies in Health Sciences of the National Institute of Biomedical Innovation; from the Ministry of Education, Science, Sports and Culture of Japan; from the Mochida Memorial Foundation for Medical and Pharmaceutical Research; and from Astellas Foundation for Research on Metabolic Disorders.

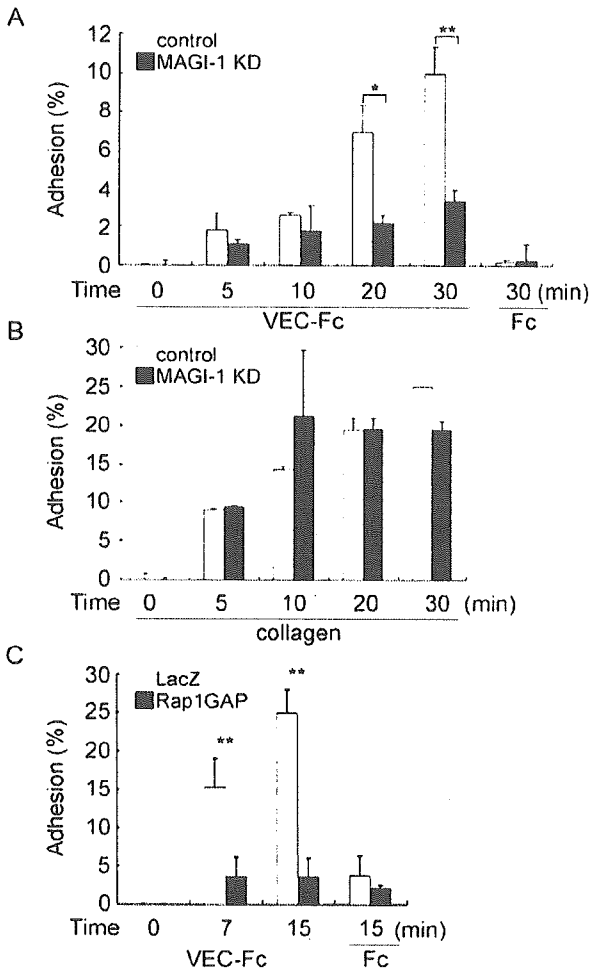

Figure 8. Depletion of MAGI-1 and inactivation of Rap1 inhibits VE-cadherin-mediated cell adhesion. (A) HUVECs transfected with control siRNAs (white column) or MAGI-1 siRNAs (black column) were cultured for 48 h, suspended in 0.5% BSA-containing medium 199, and incubated for 30 min at 37°C. Cells, 2.0×10^5, were plated onto either a VEC-Fc- or Fc-coated well for the time indicated at the bottom. Cell adhesion was quantified as described in *Materials and Methods*. The averages of triplicate (plus SDs) are presented. A representative result of three independent experiments is shown. Statistical significance was analyzed by Student's *t* test ; * $p < 0.05$ and ** $p < 0.01$. Note that adhesion of HUVECs treated with MAGI-1 siRNAs to the VEC-Fc-coated dish was significantly reduced compared with mock-treated HUVECs. (B) Adhesion of MAGI-1-depleted cells to a collagen-coated dish was comparable to mock-treated HUVECs, as analyzed by the same method described in the legend for A. (C) HUVECs infected with either LacZ-expressing adenovirus (LacZ) or Rap1GAPII-expressing virus (Rap1GAP) were analyzed for adhesion to a VEC-Fc-coated dish similarly to A.

REFERENCES

Adamsky, K., Arnold, K., Sabanay, H., and Peles, E. (2003). Junctional protein MAGI-3 interacts with receptor tyrosine phosphatase beta (RPTP beta) and tyrosine-phosphorylated proteins. J. Cell Sci. *116*, 1279–1289.

Boettner, B., Govek, E. E., Cross, J., and Van Aelst, L. (2000). The junctional multidomain protein AF-6 is a binding partner of the Rap1A GTPase and associates with the actin cytoskeletal regulator profilin. Proc. Natl. Acad. Sci. USA *97*, 9064–9069.

Boettner, B., Harjes, P., Ishimaru, S., Heke, M., Fan, H. Q., Qin, Y., Van Aelst, L., and Gaul, U. (2003). The AF-6 homolog canoe acts as a Rap1 effector during dorsal closure of the *Drosophila* embryo. Genetics *165*, 159–169.

Bos, J. L. (2005). Linking Rap to cell adhesion. Curr. Opin. Cell Biol. *17*, 123–128.

Bos, J. L., de Rooij, J., and Reedquist, K. A. (2001). Rap1 signalling: adhering to new models. Nat. Rev. Mol. Cell Biol. *2*, 369–377.

Dejana, E. (2004). Endothelial cell-cell junctions: happy together. Nat. Rev. Mol. Cell Biol. *5*, 261–270.

Dobrosotskaya, I., Guy, R. K., and James, G. L. (1997). MAGI-1, a membrane-associated guanylate kinase with a unique arrangement of protein-protein interaction domains. J. Biol. Chem. *272*, 31589–31597.

Dobrosotskaya, I. Y. (2001). Identification of mNET1 as a candidate ligand for the first PDZ domain of MAGI-1. Biochem. Biophys. Res. Commun. *283*, 969–975.

Dobrosotskaya, I. Y., and James, G. L. (2000). MAGI-1 interacts with beta-catenin and is associated with cell-cell adhesion structures. Biochem. Biophys. Res. Commun. *270*, 903–909.

Esser, S., Lampugnani, M. G., Corada, M., Dejana, E., and Risau, W. (1998). Vascular endothelial growth factor induces VE-cadherin tyrosine phosphorylation in endothelial cells. J. Cell Sci. *111*(Pt 13), 1853–1865.

Franke, B., Akkerman, J. W., and Bos, J. L. (1997). Rapid Ca2+-mediated activation of Rap1 in human platelets. EMBO J. *16*, 252–259.

Franklin, J. L., Yoshiura, K., Dempsey, P. J., Bogatcheva, G., Jeyakumar, L., Meise, K. S., Pearsall, R. S., Threadgill, D., and Coffey, R. J. (2005). Identification of MAGI-3 as a transforming growth factor-alpha tail binding protein. Exp. Cell Res. *303*, 457–470.

Fukuhara, S., Sakurai, A., Sano, H., Yamagishi, A., Somekawa, S., Takakura, N., Saito, Y., Kangawa, K., Mochizuki, N. (2005). Cyclic AMP potentiates vascular endothelial cadherin-mediated cell-cell contact to enhance endothelial barrier function through an Epac-Rap1 signaling pathway. Mol. Cell Biol. *25*, 136–146.

Fukuyama, T., Ogita, H., Kawakatsu, T., Fukuhara, T., Yamada, T., Sato, T., Shimizu, K., Nakamura, T., Matsuda, M., and Takai, Y. (2005). Involvement of the c-Src-Crk-C3G-Rap1 signaling in the nectin-induced activation of Cdc42 and formation of adherens junctions. J. Biol. Chem. *280*, 815–825.

Herren, B., Levkau, B., Raines, E. W., and Ross, R. (1998). Cleavage of beta-catenin and plakoglobin and shedding of VE-cadherin during endothelial apoptosis: evidence for a role for caspases and metalloproteinases. Mol. Biol. Cell *9*, 1589–1601.

Hirabayashi, S., Tajima, M., Yao, I., Nishimura, W., Mori, H., and Hata, Y. (2003). JAM4, a junctional cell adhesion molecule interacting with a tight junction protein, MAGI-1. Mol. Cell Biol. *23*, 4267–4282.

Hirao, K., Hata, Y., Ide, N., Takeuchi, M., Irie, M., Yao, I., Deguchi, M., Toyoda, A., Sudhof, T. C., and Takai, Y. (1998). A novel multiple PDZ domain-containing molecule interacting with N-methyl-D-aspartate receptors and neuronal cell adhesion proteins. J. Biol. Chem. *273*, 21105–21110.

Hirao, K., Hata, Y., Yao, I., Deguchi, M., Kawabe, H., Mizoguchi, A., and Takai, Y. (2000). Three isoforms of synaptic scaffolding molecule and their characterization. Multimerization between the isoforms and their interaction with N-methyl-D-aspartate receptors and SAP90/PSD-95-associated protein. J. Biol. Chem. *275*, 2966–2972.

Hogan, C., Serpente, N., Cogram, P., Hosking, C. R., Bialucha, C. U., Feller, S. M., Braga, V. M., Birchmeier, W., and Fujita, Y. (2004). Rap1 regulates the formation of E-cadherin-based cell-cell contacts. Mol. Cell Biol. *24*, 6690–6700.

Hudry-Clergeon, H., Stengel, D., Ninio, E., and Vilgrain, I. (2005). Platelet-activating factor increases VE-cadherin tyrosine phosphorylation in mouse endothelial cells and its association with the PtdIns3′-kinase. FASEB J. *19*, 512–520.

Hung, A. Y., and Sheng, M. (2002). PDZ domains: structural modules for protein complex assembly. J. Biol. Chem. *277*, 5699–5702.

Ide, N., Hata, Y., Deguchi, M., Hirao, K., Yao, I., and Takai, Y. (1999). Interaction of S-SCAM with neural plakophilin-related Armadillo-repeat protein/delta-catenin. Biochem. Biophys. Res. Commun. *256*, 456–461.

Iyer, S., Ferreri, D. M., DeCocco, N. C., Minnear, F. L., and Vincent, P. A. (2004). VE-cadherin-p120 interaction is required for maintenance of endothelial barrier function. Am. J. Physiol Lung Cell Mol. Physiol. *286*, L1143–L1153.

Kawajiri, A., Itoh, N., Fukata, M., Nakagawa, M., Yamaga, M., Iwamatsu, A., and Kaibuchi, K. (2000). Identification of a novel beta-catenin-interacting protein. Biochem. Biophys. Res. Commun. *273*, 712–717.

Knox, A. L., and Brown, N. H. (2002). Rap1 GTPase regulation of adherens junction positioning and cell adhesion. Science *295*, 1285–1288.